The HERMES Spectrometer

K. Ackerstaff[5], A. Airapetian[30], N. Akopov[30], M. Amarian[30], V. Andreev[24], E.C. Aschenauer[11,21], R. Avakian[30], H. Avakian[9], A. Avetissian[30], B. Bains[13], S. Barrow[23], W. Beckhusen[5], M. Beckmann[10], St. Belostotski[24], E. Belz[4], Th. Benisch[8], S. Bernreuther[8], N. Bianchi[9], J. Blouw[21], H. Böttcher[6], A. Borissov[6,12], J. Brack[4], B. Braun[8,19], B. Bray[3], S. Brons[6,27], W. Brückner[12], A. Brüll[12], H.J. Bulten[15], G.P. Capitani[9], P. Carter[3], P. Chumney[20], E. Cisbani[25], S. Clark[4], S. Colilli[25], H. Coombes[1], G.R. Court[14], P. Delheij[27], E. Devitsin[18], C.W. de Jager[21], E. De Sanctis[9], D. De Schepper[2,17], P.K.A. de Witt Huberts[21], P. Di Nezza[9], M. Doets[21], M. Düren[8], A. Dvoredsky[3], G. Elbakian[30], J. Emerson[26,27], A. Fantoni[9], A. Fechtchenko[7], M. Ferstl[8], D. Fick[16], K. Fiedler[8], B.W. Filippone[3], H. Fischer[10], H.T. Fortune[23], J. Franz[10], S. Frullani[25], M.-A. Funk[5], N.D. Gagunashvili[7], P. Galumian[1], H. Gao[13], Y. Gärber[6], F. Garibaldi[25], G. Gavrilov[24], P. Geiger[12], V. Gharibyan[30], V. Giordjian[9], F. Giuliani[25], A. Golendoukhin[16], B. Grabowski[5], G. Graw[19], O. Grebeniouk[24], P. Green[1,27], G. Greeniaus[1,27], M. Gricia[25], C. Grosshauser[8], A. Gute[8], J.P. Haas[20], K. Hakelberg[5], W. Haeberli[15], J.-O. Hansen[2], D. Hasch[6], O. Hausser† [26,27], R. Henderson[27], Th. Henkes[21], R. Hertenberger[19], Y. Holler[5], R.J. Holt[13], H. Ihssen[5], A. Izotov[24], M. Iodice[25], H.E. Jackson[2], A. Jgoun[24], C. Jones[2], R. Kaiser[26,27], J. Kelsey[17], E. Kinney[4], M. Kirsch[8], A. Kisselev[24], P. Kitching[1], H. Kobayashi[28], E. Kok[21], K. Königsmann[10], M. Kolstein[21], H. Kolster[19], W. Korsch[3], S. Kozlov[24], V. Kozlov[18], R. Kowalczyk[2], L. Kramer[17], B. Krause[6], A. Krivchitch[24], V.G. Krivokhijine[7], M. Kueckes[27], P. Kutt[23], G. Kyle[20], W. Lachnit[8], R. Langstaff[27], W. Lorenzon[23], M. Lucentini[25], A. Lung[3], N. Makins[2], V. Maleev[24], S.I. Manaenkov[24], K. Martens[1], A. Mateos[17], K. McIlhany[3], R.D. McKeown[3], F. Meißner[6], F. Menden[27], D. Mercer[4], A. Metz[19], N. Meyners[5], O. Mikloukho[24], C.A. Miller[1,27], M.A. Miller[13], R. Milner[17], V. Mitsyn[7], G. Modrak[6], J. Morton[14], A. Most[13], R. Mozzetti[9], V. Muccifora[9], A. Nagaitsev[7], Y. Naryshkin[24], A.M. Nathan[13], F. Neunreither[8], M. Niczyporuk[17], W.-D. Nowak[6], M. Nupieri[9], P. Oelwein[12], H. Ogami[28], T.G. O'Neill[2], R. Openshaw[27], V. Papavassiliou[20], S.F. Pate[17,20], S. Patrichev[24], M. Pitt[3], H.J. Plett[8], H.R. Poolman[21], S. Potashov[18], D. Potterveld[2], B. Povh[12], V. Prahl[5], G. Rakness[4], V. Razmyslovich[24], R. Redwine[17], A.R. Reolon[9], R. Ristinen[4], K. Rith[8], H.O. Roloff[6], G. Röper[5], P. Rossi[9], S. Rudnitsky[23], H. Russo[8], D. Ryckbosch[11], Y. Sakemi[28], F. Santavenere[25], I. Savin[7], F. Schmidt[8], H. Schmitt[10], G. Schnell[20], K.P. Schüler[5], A. Schwind[6], T.-A. Shibata[28], T. Shin[17], B. Siebels[1], A. Simon[10,20], K. Sinram[5], W.R. Smythe[4], J. Sowinski[12], M. Spengos[23], K. Sperber[5], E. Steffens[8], J. Stenger[8], J. Stewart[14], F. Stock[8,12], U. Stößlein[6], M. Sutter[17], H. Tallini[14], S. Taroian[30], A. Terkulov[18], D. Thiessen[26,27], B. Tipton[17], V. Trofimov[24], A. Trudel[27], M. Tytgat[11], G.M. Urciuoli[25], R. Van de Vyver[11], J.F.J. van den Brand[21,29], G. van der Steenhoven[21], J.J. van Hunen[21], D. van Westrum[4], A. Vassiliev[24], M.C. Vetterli[26,27], M.G. Vincter[27], E. Volk[12], W. Wander[8], T.P. Welch[22], S.E. Williamson[13], T. Wise[15], G. Wöbke[5], K. Woller[5], S. Yoneyama[28], K. Zapfe-Düren[5], T. Zeuli[2], H. Zohrabian[30],

[1]Department of Physics, University of Alberta, Edmonton, Alberta T6G 2N2, Canada
[2]Physics Division, Argonne National Laboratory, Argonne, IL 60439, USA
[3]W.K.Kellogg Radiation Lab, California Institute of Technology, Pasadena, CA, 91125, USA
[4]Nuclear Physics Laboratory, University of Colorado, Boulder CO 80309-0446, USA
[5]DESY, Deutsches Elektronen Synchrotron, 22603 Hamburg, Germany
[6]DESY, 15738 Zeuthen, Germany
[7]Joint Institute for Nuclear Research, 141980 Dubna, Russia
[8] Physikalisches Institut, Universität Erlangen-Nürnberg, 91058 Erlangen, Germany
[9]Istituto Nazionale di Fisica Nucleare, Laboratori Nazionali di Frascati, I-00044 Frascati, Italy
[10] Fakultät für Physik, Universität Freiburg, 79104 Freiburg, Germany
[11]Department of Subatomic and Radiation Physics, University of Gent, 9000 Gent, Belgium
[12]Max-Planck-Institut für Kernphysik, 69029 Heidelberg, Germany
[13]Department of Physics, University of Illinois, Urbana, IL 61801, USA

[14]Physics Department, University of Liverpool, Liverpool L69 7ZE, United Kingdom
[15]Department of Physics, University of Wisconsin-Madison, Madison, WI 53706, USA
[16]Physikalisches Institut, Philipps-Universität Marburg, 35037 Marburg, Germany
[17]Laboratory for Nuclear Science, Massachusetts Institute of Technology, Cambridge, MA 02139, USA
[18]Lebedev Physical Institute, 117924 Moscow, Russia
[19] Sektion Physik, Universität München, 85748 Garching, Germany
[20]Department of Physics, New Mexico State University, Las Cruces, NM 88003, USA
[21]Nationaal Instituut voor Kernfysica en Hoge-Energiefysica (NIKHEF), 1009 DB Amsterdam, Netherlands
[22]Department of Physics, University of Oregon, Eugene, OR 97403 USA
[23]Department of Physics, University of Pennsylvania, Philadelphia PA 19104-6396, USA
[24]Petersburg Nuclear Physics Institute, St.Petersburg, 188350 Russia
[25]Istituto Nazionale di Fisica Nucleare, Sezione Sanità, 00161 Roma, Italy
[26]Department of Physics, Simon Fraser University, Burnaby, British Columbia V5A 1S6 Canada
[27]TRIUMF, Vancouver, British Columbia V6T 2A3, Canada
[28]Department of Physics, Tokyo Institute of Technology, Tokyo 152, Japan
[29] Department of Physics and Astronomy, Vrije Universiteit, 1081 HV Amsterdam, The Netherlands.
[30]Yerevan Physics Institute, 375036, Yerevan, Armenia

Abstract

The HERMES experiment is collecting data on inclusive and semi-inclusive deep inelastic scattering of polarised positrons from polarised targets of H, D, and ^{3}He. These data give information on the spin structure of the nucleon. This paper describes the forward angle spectrometer built for this purpose. The spectrometer includes numerous tracking chambers (micro-strip gas chambers, drift and proportional chambers) in front of and behind a 1.3 T.m magnetic field, as well as an extensive set of detectors for particle identification (a lead-glass calorimeter, a pre-shower detector, a transition radiation detector, and a threshold Čerenkov detector). Two of the main features of the spectrometer are its good acceptance and identification of both positrons and hadrons, in particular pions. These characteristics, together with the purity of the targets, are allowing HERMES to make unique contributions to the understanding of how the spins of the quarks contribute to the spin of the nucleon.

(Submitted to Nuclear Instruments and Methods)

1 Introduction.

The HERMES experiment (HERA MEasurement of Spin) is a second generation polarised deep inelastic scattering (DIS) experiment to study the spin structure of the nucleon. It is being run at the HERA storage ring at DESY[1].

Several experiments over the last decade have provided accurate data on the polarisation asymmetry of the cross-section for *inclusive* scattering where only the scattered lepton is detected. These experiments have been interpreted as showing that at most 30% of the nucleon spin comes from the spins of the quarks. Further knowledge of the origin of the nucleon's spin can be gained by studying *semi-inclusive* processes involving the detection of hadrons in coincidence with the scattered lepton. These data offer a means of 'flavour-tagging' the struck quark to help isolate the contributions to the nucleon spin of the individual quark flavours, including the sea quarks. The interpretation of semi-inclusive data is made clearer if the type of hadron is identified. This is a central theme of the HERMES experiment, which can identify pions and will add kaon identification for 1998.

The physics program for HERMES is very broad. The experiment contributes inclusive data with qualitatively different systematic uncertainties to improve the world data set for the x dependence and the integral of the spin structure function $g_1(x)$ for both the proton and the neutron (see below for the definition of x). Most importantly, HERMES is providing new precise data on semi-inclusive processes by virtue of the good acceptance of the spectrometer combined with hadron identification and the purity of the targets.

The HERA storage ring can be filled with either electrons or positrons, which are accelerated to 27.5 GeV. Positrons have been used since 1995 because longer beam lifetimes are then possible. Since with few exceptions such as the luminosity measurement, the physics processes are the same for positrons and electrons, the term "positron" will be used for both in this paper.

In addition to studying polarised DIS using $\vec{\mathrm{H}}, \vec{\mathrm{D}}$, and $^3\vec{\mathrm{He}}$ targets, data are collected with unpolarised gases ($\mathrm{H}_2, \mathrm{D}_2, ^3\mathrm{He}, \mathrm{N}_2$). This provides in a relatively short period of time (2-3 weeks) high statistics data sets that are used to study important properties of the nucleon not related to spin, such as the flavour asymmetry of the sea, as well as hadronisation in nuclei.

[1] HERA is an e-p collider but only the e beam is used by HERMES

2 General Description.

The HERMES experiment is located in the East hall of the HERA storage ring complex at DESY. The spectrometer is a forward angle instrument of conventional design. It is symmetric about a central, horizontal shielding plate in the magnet. Due to this symmetry, the description of the detectors contained in this paper will apply typically to only one half of the spectrometer, in particular with respect to the number of detectors quoted and their dimensions. A diagram of the spectrometer is shown in Fig. 1. The coordinate system used by HERMES has the z axis along the beam momentum, the y axis vertical upwards, and the x axis horizontal, pointing towards the outside of the ring. The polar (θ) and azimuthal (ϕ) scattering angles as well as the initial trajectory for the determination of the particle's momentum are measured by the front tracking system, which consists of microstrip gas chambers (MSGC, referred to as the vertex chambers (VC)) and drift chambers (DVC, FC1/2). The momentum measurement is completed by two sets of drift chambers behind the magnet (BC1/2 and BC3/4). In addition, there are three proportional chambers in the magnet (MC1/3) to help match front and back tracks as well as to track low momentum particles that do not reach the rear section of the spectrometer.

Particle identification (PID) is provided by a lead-glass calorimeter, a pre-shower detector (H2) consisting of two radiation lengths of lead followed by a plastic scintillator hodoscope, a transition radiation detector (TRD) consisting of six identical modules, and a threshold Čerenkov detector (Č). The particle identification system was designed to provide a hadron rejection factor of 10^4 to yield a very clean DIS positron sample, and exceeds this in practice. Pion identification is provided by a threshold Čerenkov detector. An upgrade to a ring imaging Čerenkov detector that will identify both pions and kaons is being prepared for operation in 1998. The calorimeter and pre-shower detector are included in the trigger along with a second hodoscope (H1) placed in front of the TRD. An additional trigger hodoscope (H0) was included in 1996 in front of FC1 to reduce the trigger rate from background caused by the proton beam.

The acceptance is limited at small angles by an iron

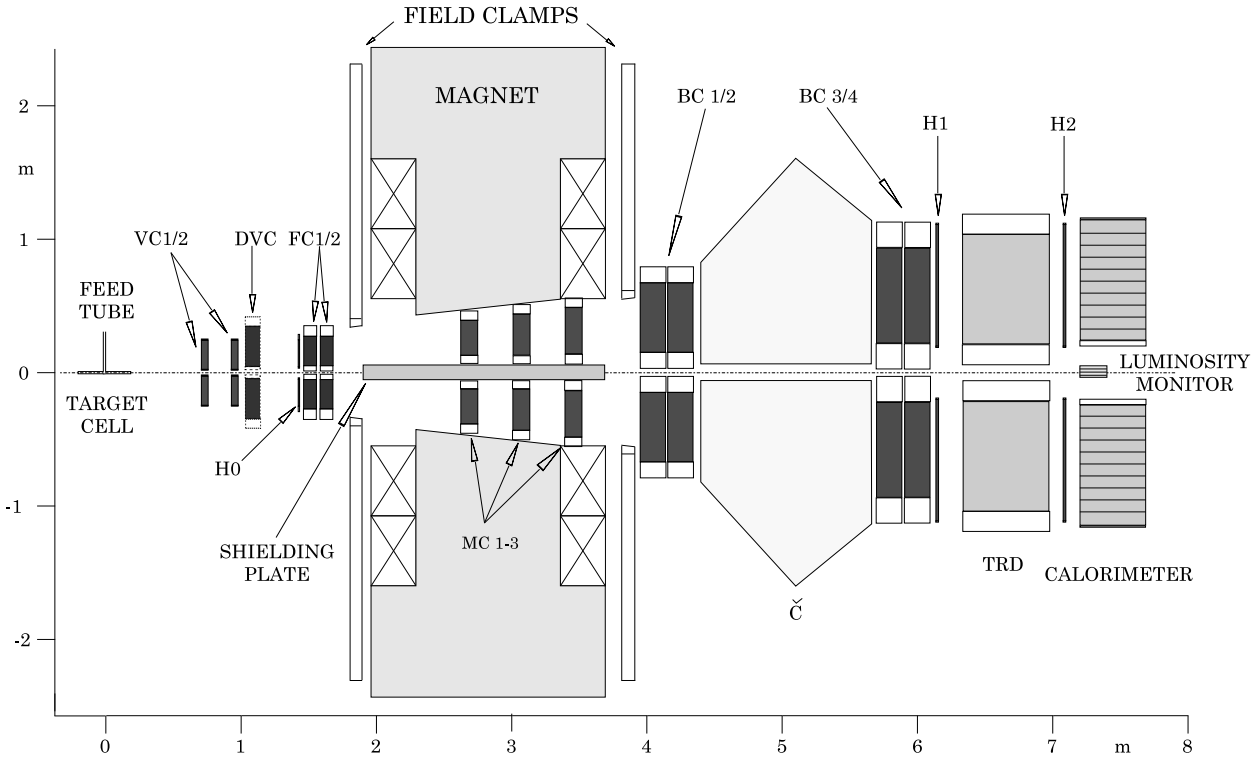

Figure 1: Schematic side view of the HERMES spectrometer. See the text for the meaning of the labels.

plate in the beam plane, which shields the positron and proton beams from the magnetic field of the spectrometer magnet. Both beams go through the spectrometer, separated by 72 cm. Particles with scattering angles within ±170 mrad in the horizontal direction and between +(−)40 mrad and +(−)140 mrad in the vertical direction are accepted. Therefore, the range of scattering angles is 40 mrad to 220 mrad. Spin structure functions depend on x (x= $Q^2/2M\nu$ where Q is the four-momentum transfer in the DIS reaction, ν is the energy transfer, and M is the mass of the nucleon). The variable x can be interpreted as the fraction of the nucleon's momentum carried by the struck quark. The x range covered by the HERMES experiment is 0.02-1.0, although there is little count rate for x$\geq$0.8 when W $>$ 2 GeV (W is the photon-nucleon invariant mass).

The experiment is mounted on a large platform that can move on rails together with an attached trailer (ET) containing the electronics and the gas systems. A fixed but removable concrete wall between the platform and the ET shields the main part of the hall from radiation and hence allows access to the electronics while the accelerators are running. Cables and gas pipes between the detectors and the ET are routed beneath the platform to a large cable tray passing under the shielding wall. The experiment was assembled in the East hall outside the shielding during the 1994 HERA run. After the shielding wall had been dismantled, the platform/trailer was moved into place in the ring. The shielding wall was re-erected between the platform and the electronics trailer in such a way that the experiment could be moved far enough within the shielding to allow the HERA maintenance tram access to the tunnel on 24 hours notice.

3 The Target Region.

The HERMES target consists of gas from a polarised source fed into a storage cell internal to the HERA positron ring. In 1995, an optically pumped polarised $^3\vec{\mathrm{H}}\mathrm{e}$ cell was used to supply gas to the storage cell [1], while an atomic beam source (ABS) was used in 1996-97 to produce a $\vec{\mathrm{H}}$ target [2]. The ABS will be modified for operation with $\vec{\mathrm{D}}$ in 1998-99. It is also possible to inject unpolarised gases into the storage

cell. The following were used in the first three years of operation: $H_2, D_2, {}^3He, N_2$.

The target region is shown schematically in Fig. 2. The gas enters an open-ended (ie. windowless) T-shaped tube that confines the gas atoms in a region around the positron beam. The storage cell increases the areal target density by about two orders of magnitude compared to a free atomic beam. The gas atoms leak out the open ends of the target cell and are pumped away by a high speed differential pumping system. In this way, the number of atoms seen at the target location by the beam is maximized while minimizing the effect on the stored beam. The storage cell is an elliptical tube, 9.8 mm high by 29.0 mm wide and 400 mm in length. It was made of 125 μm thick ultra-pure aluminium in 1995 and 75 μm aluminium in 1996-97. The transition from the cell to the beam pipe was made smooth to avoid the generation of wake fields that could cause heating and increase the emittance of the beam. This was accomplished using thin perforated tubes called "wake field suppressors".

The amount of synchrotron radiation created upstream of the HERMES area is considerable, even though it is reduced by the addition of two weak dipoles downstream of the last bending magnet in the arc of the accelerator. If it were allowed to hit the target cell, it would damage the cell coating, and on the order of 10^{13} - 10^{14} soft synchrotron photons per second would Compton scatter into the spectrometer acceptance. This is prevented by a system of two collimators installed near the target. C1 is placed 2 m upstream of the target and protects the next collimator from direct radiation. It actually consists of two moveable collimators, C1H in the horizontal direction and C1V in the vertical, separated by 0.5 m. These collimators are opened during beam injection and operated at a narrow but safe setting (15σ + 0.5 mm) during HERMES operation. During the first three years of operation, typical beam parameters were σ_x= 0.31 mm and σ_y= 0.07 mm. C2 has a fixed aperture that is slightly larger than C1, and is located right in front of the storage cell to protect it from photons scattered in C1. It also protects the cell from direct radiation during beam injection. Note that only C2 is shown in Fig. 2.

Particles scattered into the spectrometer acceptance exit the target chamber through a thin (0.3 mm) stainless steel foil. Background from showers (initiated mostly by γ's from π^0 decay) is reduced by also making the beam pipe just downstream of the target chamber of thin stainless steel.

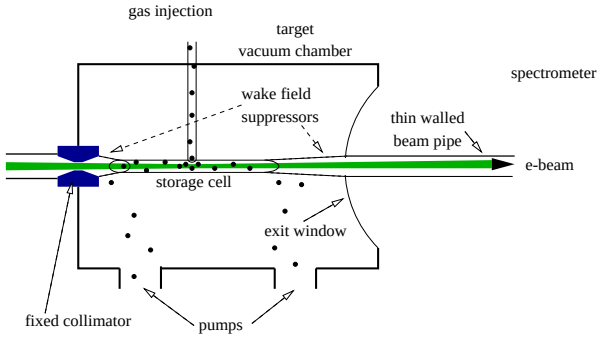

Figure 2: Schematic of the target region. See the text for more explanation.

4 The Magnet.

The HERMES spectrometer magnet is of the H-type with field clamps in front as well as behind in order to reduce the fringe fields at the position of the drift chambers FC2 and BC1. A massive iron plate in the symmetry plane shields the positron and proton beams as they pass through the magnet.
The most important features of the magnet are:

- It is capable of providing a deflecting power of $\int Bdl$ = 1.5 T·m, although it is operated at 1.3 T·m to reduce power consumption. The smaller field integral does not significantly impair the performance of the spectrometer. The variation of the deflecting power within the acceptance is less than 10 %.

- The gap between the pole faces encloses the geometrical acceptance of $\pm$(40..140) mrad in the vertical direction. In the horizontal direction $\pm$170 mrad plus another $\pm$100 mrad starting halfway through the magnet is provided. The pole faces are tilted parallel to the limits of the vertical angular acceptance. Due to the limited space of 8.5 m for the HERMES spectrometer between the center of the target and the first quadrupole magnet of the electron machine, only 2.2 m between the drift chambers FC2 on the front and BC1 on the rear side are utilized for the magnet.

- The fringe field at the positions of the adjacent drift chambers does not exceed 0.1 T.

- An effective magnetic shielding substantially reduces the effect of the magnet on the proton and positron beams. In particular, the sextupole moment of the magnetic field in the beam tubes is minimized.

- A correction coil with a deflecting power of 0.08 T·m is accommodated inside the shielding of the positron beam pipe. This coil is used to correct for fringe fields and the imperfections of the magnetic shielding in this section of the iron plate. It is also intended to compensate the transverse holding field of the target when operating with transverse polarisation. It serves as an element of a closed orbit bump with no net global effect on the positron beam.

Magnetic model calculations were done with the 3D-codes MAFIA [3] and TOSCA [4]. The calculations agree with subsequent magnetic measurements within a few percent. The field measurements were done with a 3D-Hall probe on an automated 3D-mapping machine. The results exhibit an overall reproducibility of about 10^{-3}, and a field pattern as expected. No homogeneous regions are found due to the high gap to length ratio of the magnet, and a pronounced step in the field is observed that reflects the structure of the iron shielding plate. The detailed field map was integrated into the track reconstruction algorithm, as described later.

5 The Tracking System

The tracking system serves several functions, which vary somewhat in their performance requirements:

- Determine the event vertex in the target cell to ensure that reconstructed events come only from the sub-mm beam envelope in the target gas, with the expected z-distribution. Also, the analysis of events with multiple tracks requires either a common vertex, or possibly an additional displaced vertex for a reconstructed particle decay.

- Measure the scattering angles for kinematic reconstruction.

- Measure the particle momentum from the track deflection in the spectrometer dipole magnet.

- Identify the hits in the PID detectors associated with each track.

When all tracking detectors are fully operational, the momentum resolution for positrons is limited by Bremsstrahlung in the material of the target cell walls, the 0.3 mm thick stainless steel vacuum window, as well as the first tracking detectors. Even the resolution in scattering angle is normally limited by multiple scattering in this material. An exception was 1995, the first year of operation, when the low efficiency of most planes of the Vertex Chambers (improved for 1996 for the top detector) made it more attractive to reconstruct the tracks using only the drift chambers (DC), as will be explained later in more detail. This mode of operation resulted in the resolution of reconstructed kinematic quantities being much more sensitive to the DC spatial resolution.

The locations of the tracking detectors are shown in Fig. 1 and listed in Table 1, which also summarizes their properties.

The microstrip gas counters VC1/2, the drift vertex chambers DVC's, and the front drift chambers FC1/2 provide both vertex reconstruction to the target, and definition of the scattering angle. In conjunction with the front tracking, the back drift chambers BC1/2 and BC3/4 measure the magnetic deflection and hence the momentum. The BC's also identify the cells in the PID detectors associated with each track. The proportional chambers inside the magnet (MC1/3) were originally intended to ensure that multi-track ambiguities could be resolved. As it happens, chamber occupancies are low enough that this can be accomplished using the drift chambers alone. However, the MC's are found to be very useful for momentum analysis of low energy decay products that are deflected too much to reach the downstream tracking detectors.

The horizontal length of the BC's precluded the use of long horizontal wires for y measurements. Hence all planes are one of three types with wires oriented either in the vertical (for X measurement), or tilted 30° right or left (U and V planes). In order to allow the use of fast reconstruction algorithms, all tracking detectors are restricted to this geometry. Like the rest of the spectrometer, the tracking system is symmetric about the beam plane.

5.1 Vertex Chambers

The purpose of the vertex chambers is to provide high-precision measurements of the scattering angle and the vertex position over the full acceptance of the experiment, in the presence of a significant back-

CHAMBER	Vertex		Drift Vertex	Front		Magnet			Back	
Detector name	VC1	VC2	DVC	FC1	FC2	MC1	MC2	MC3	BC1/2	BC3/4
mm from target	731	965	1100	1530	1650	2725	3047	3369	4055	5800
Active Area:										
Horizontal (mm)	323	393	474	660	660	996	1210	1424	1880	2890
Vertical (mm)	137	137	290	180	180	263	306	347	520	710
Cell design	microstrip gas		horizontal-drift	horizontal-drift			MWPC		horizontal-drift	
Cell width (mm)	0.193		6	7			2		15	
A-C plane gap (mm)	3		3	4			4		8	
Anode (A) material	200 μm glass(Al)		W(Au)	W(Au)			W(Au)		W(Au)	
Anode wire diameter	7 μm		30 μm	20 μm			25 μm		25 μm	
Potential wire mat'l	Al strip		Be-Cu(Au)	Al(Au)					Be-Cu(Au)	
Potential wire dia.	85 μm		50 μm	50 μm					127 μm	
Cathode (C) material	Al on glass		Al on Mylar	Al on Mylar		Be-Cu wires			C on Kapton	
Cathode thickness	200 μm		34 μm	6.4 μm		90 μm @ 0.5 mm pitch			25.4 μm	
Gas composition:	DME/Ne		$Ar/CO_2/CF_4$	$Ar/CO_2/CF_4$		$Ar/CO_2/CF_4$			$Ar/CO_2/CF_4$	
(%)	50/50		90/5/5	90/5/5		65/30/5			90/5/5	
U,V stereo angle	$+5°, -90°$		$\pm 30°$	$\pm 30°$		$\pm 30°$			$\pm 30°$	
Resolution/plane (σ)	65 μm		220 μm	225 μm		700 μm			275 μm	300 μm
Wires in X plane	1674	2046	80	96	96	496	608	720	128	192
Wires in U,V plane	2170	2170	96	96	96	512	608	720	128	192
Module config.	VUX	XVU	XX'UU'VV'	UU'XX'VV'			UXV		UU'XX'VV'	
Rad. length/module	0.8%		0.25%	0.075%			0.29%		0.26%	
Number of modules (upper or lower)	1	1	1	1	1	1	1	1	2	2
Channels/module	6014	6386	544	576	576	1520	1824	2160	768	1152
Total channels	24800		1088	2304			11008		7680	

Table 1: Tracking Chamber properties.

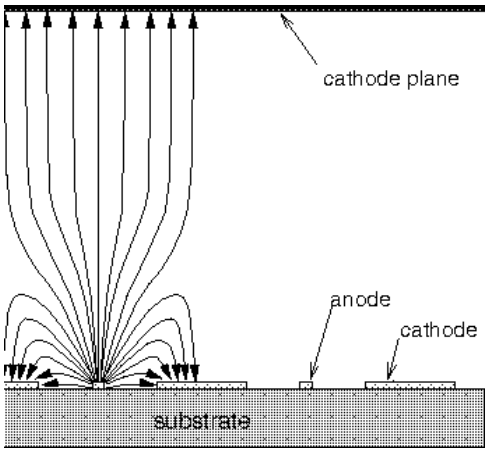

Figure 3: Schematic view of a drift cell in a MicroStrip Gas Counter, showing the field lines. This figure has been taken from ref.[6].

ground flux. The proximity of the VC to the target implies that at the minimum scattering angle, the tracks from the downstream end of the target cell pass the VC active area 20 mm from the beam axis, or only 5 mm from the beam tube. In combination with the need to minimize high-Z materials near the beam tube that could convert the numerous photons from π^0 decay into high multiplicity showers, this geometry presented severe problems in mechanical design that would have been very difficult to solve in the context of wire chamber frames. All these requirements are met through the use of a relatively new technology, a microstrip gas chamber (MSGC). In this technique [5], metal strips are etched on a thin, semi-rigid substrate of high resistivity, allowing for higher drift fields and much smaller cell pitch than in a conventional drift chamber. Each of the upper and lower VC assemblies contains six MSGC planes, grouped into two "modules" (VUX and XUV for VC1 and VC2 respectively), which are sufficiently separated to provide a precise determination of the front track by the VC alone. The total radiation length of one module is 0.8% X_0 and the thickness of the target chamber vacuum window is 1.7% X_0, so that for momenta below about 7 GeV the angular accuracy becomes limited by multiple scattering. An inherent cost associated with the MSGC choice is the large channel count – 24,800 channels in total. This requires a highly integrated readout system, including analog electronic signal storage on the planes and multiplexed digitization at the detector.

The basic features of the MSGC drift cell are shown in Fig. 3. Ionization electrons created by a traversing particle in a 3 mm thick gas volume move in a drift field of about 5 kV/cm directly away from a planar cathode and towards a 200 μm thick glass substrate that carries a pattern of fine etched aluminum strips. The field is produced by a 1800 V potential on the cathode planes. A voltage difference of 580 V is applied between the 7 μm wide anode strips and the 85 μm wide cathode strips forming the pattern on the substrates. As a result, gas multiplication occurs in the vicinity of the anode, a process comparable to that in a wire chamber. High gas amplification at 580V is obtained by using a DiMethyl-Ether(DME)/Ne mixture (50/50%). The gas gain is set at a level such that the signals are about three times that of silicon detectors of the same material thickness, leading to a better signal to noise ratio. Even with only single bit per cell digital read-out, a spatial resolution much better than the cell pitch is achieved, due to charge sharing between cells.

The metallic strip pattern that creates the electrical field configuration is carried on substrates, the material of which is a critical choice. Low Z is preferred to minimize the effects of multiple scattering and Bremsstrahlung. Surface properties are important as electrons, ions, and gas pollutants may stick and cause field modifications, discharges, ageing, and radiation damage. Since part of the avalanche falls on the substrate instead of on the conductive strip, the substrate should have a certain degree of conductivity in order to remove the collected surface charge. D-263 glass was chosen as the substrate material [7]. It consists of SiO_x (64.1 %), Al_2O_3 (4.5 %), K_2O (6.6 %), TiO (4.2 %), ZnO (6.1 %), Na (6.1 %), with the remainder (8.4 %) unspecified. It has a bulk resistivity of 10^{15} Ωcm, equivalent to a surface resistivity of 10^{17} $\Omega/\Box$, caused by the migration of electrons and Na^+ ions. The thickness of the substrates is 0.2 mm, the minimum required for safe handling and to have sufficient rigidity to resist electrostatic distortions.

The active area of the U or V planes is as large as 484×137 mm^2. The largest substrate area that could be processed is 150 × 200 mm^2. Therefore, 5 substrates are combined to form one 30° plane. The substrates are cut along the cathode strip, and glued on a carrier frame, leading to a gap of on average 461 μm between the anode wires of consecutive substrates. No loss in efficiency at these boundaries has been observed.

The PC carrier frame to which the substrates are

glued has sufficient mechanical stiffness to be self-supporting. The carrier frames are mounted in a fixture attached to the inside of the lid of the box that acts as the gas enclosure. The fixture provides a means of precisely aligning the planes with respect to fiducials on the outside of the lid. The wall of the box, which is shaped to curve around the beam tube, is only 0.5 mm thick and made of low-Z material. The thin windows for the detected particles have two layers enclosing non-flammable flush gas to ensure no leaks of flammable gas.

In order to minimize external data flow, digitization of the signals is done in an electronic assembly mounted on the detector. The high degree of digitizer multiplexing required for economy is made possible by continuously storing the charge buckets collected by each anode strip in a switched-capacitor analog pipeline. There are 64 preamplifiers and pipelines, each 32 steps deep, integrated on each Analog Pipeline Chip (APC). The pipelines are clocked with the HERA bunch frequency (10.4 MHz). If an event trigger occurs any time within 3.1 μs (32 $\times$ 96 ns) after an event, the pipelines are stalled before the data are shifted out and lost. The pipelines are advanced until the buckets of interest in the vicinity of the bunch causing the trigger are about to appear at the pipeline output stage. Then the pipelines are shifted much more slowly as the buckets of interest are presented to the "tracking discriminators", which were designed to compensate the rising baseline of the APC chip. A sample and hold circuit is used to keep the threshold at a fixed value above the baseline offset, given by the readout value of the previous channel. If a hit is detected, the baseline restore operation is suspended, until the following channel no longer exceeds the discriminator level. For that reason, the system is limited to handle a maximum cluster size of up to four neighboring anode strips. The first two channels of each chip are not connected to an anode strip, and serve as a reference for the baseline restoration. The data from each discriminator (62 channels) are stored in its shift register. As soon as all digital data have been stored, the inputs of the APC chips are enabled and a new trigger can be accepted. The dead time during readout of the APC chips and digitization into the shift register is 56 μs. Simultaneously, serial readout of the shift registers is started. Addresses of signals above threshold are loaded into memory stacks. If during this operation a new trigger arrives, the new event waits in the APC pipeline until the data of the previous event are transferred into the memory stacks. Subsequently, the memory stacks are read out serially via a data driver into a Struck ECL300 FASTBUS module.

The efficiency of the vertex detector is measured in two ways. In the internal tracking approach, tracks are identified using VC data alone, requiring hits in five of six planes. The track is reconstructed from four planes, and a hit is accepted in the fifth plane if it is within 200 μm of the track. Only tracks are considered that point to the target and are reconstructable by the rest of the tracking system. The efficiency of the fifth plane is then defined as the fraction of events with a hit close to the track. In the external tracking approach, the efficiency is determined with tracks reconstructed using the drift chamber system, extrapolated to the vertex chamber. In both cases, efficiencies in the range 60-90% were found for the 1995 data, where a prototype version of the APC chip was used that exhibited a strongly non-linear baseline. This caused high noise. Due to the fragility of some of the anode resistors that were etched on the substrates, the high voltage could not be raised sufficiently to get a high enough signal-to-noise ratio. For 1996 running, the substrates and APC chips of the upper chamber were replaced, resulting in much improved efficiencies of around 95%. The lower half was similarly upgraded for 1997 running. The resolution has been determined by comparing the distance between the track, formed with 5 planes, and the hit in the sixth plane, and also by comparing the horizontal angle of the track calculated from the X planes with that from the U and V planes. Both methods yield a resolution of about 65 μm (σ) per plane.

The vertex reconstruction capability of the VC is illustrated in Fig. 4, which is a histogram of the transverse coordinates of the point of closest approach of two tracks in an event. A well defined beam envelope is seen. Furthermore, the figure shows that the vertices are well separated from the target cell wall represented by the ellipse.

Over three years of operation, there has been no observed degradation of performance that would suggest ageing effects.

5.2 The Drift Chambers

The drift chambers DVC, FC1/2, BC1/2 and BC3/4 are of the conventional horizontal-drift type. Each layer of drift cells consists of a plane of alternating anode and cathode wires between a pair of cathode foils. The cathode wires and foils are at negative

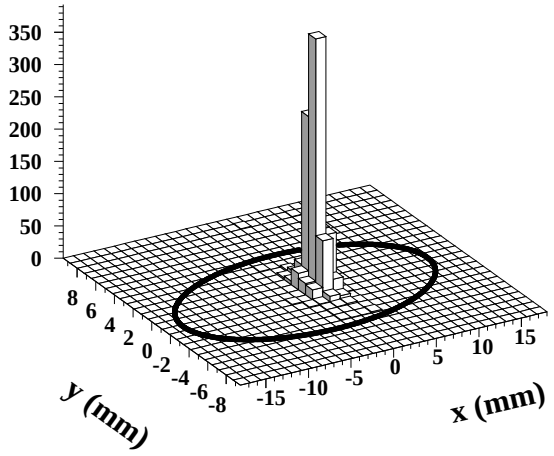

Figure 4: Vertex reconstruction in the transverse coordinates using the VC alone. This plot was made using two-track events only to get a well defined vertex. The outline of the target cell is shown as the ellipse.

high voltage with the anode sense wires at ground potential. The chambers are assembled as modules consisting of six such drift cell layers in three coordinate doublets (UU', XX' and VV'). The wires are vertical for the X planes and at an angle of $\pm 30°$ to the vertical for the U and V planes. The X', U' and V' planes are staggered with respect to their partners by half the cell size in order to help resolve left-right ambiguities. Each sense plane consists of a fiberglass-epoxy frame laminated to a printed circuit board (PCB) that has solder pads for the wires. Except in the case of the DVC's, the PCB's carry the traces leading past O-ring gas seals to external connectors. The opposite ends of the cathode wires connect to internal distribution buses for the negative high voltage. Each module is enclosed between metallized Mylar gas windows mounted on metal frames. Identical modules are situated above and below the beam pipe.

The frames of all the drift chambers except the DVC's have sufficient length to allow both ends of all wires in the U and V planes to terminate on the long edges of the frames. Hence all U and V wires and their PCB traces have the same length and similar capacitance. The onboard electronics are mounted along only the one long edge opposite to the beam pipes. This arrangement does not sacrifice mechanical stiffness of the frame. Since the inside aperture of each frame is only as large as the active area in common with all the frames, each stressed frame member is as short as possible. A shallow relief is milled in the inactive end regions of the U and V frames to allow the wires to stand off from the frame material. Proximity to the beam of the active areas of all chambers required external notches to be machined in the frames to accommodate the beam pipes. As these notches are short, they do not seriously compromise the mechanical stiffness of the frames.

The choice of gas mixture for the drift chambers was governed by the serious inconvenience of controlling the hazards of a flammable gas in a tunnel environment. As well, there is an advantage in limiting the drift cell occupation time and hence the number of extraneous hits that must be accommodated in track finding. The mixture Ar(90%)/CO_2(5%)/CF_4(5%) is both fast and non-flammable [8]. Its drift velocity has been measured as a function of field - eg. > 7 cm/μsec at E=800 V/cm [9]. FC2 and BC1 operate in a dipole fringe field that reaches 0.1 T. Mixtures containing CF_4 have been shown to result in compromised resolution due to electron attachment [10], and large Lorentz drift angles in magnetic fields. However, they have the advantages of short occupation time and long chamber lifetime [11].

The gas pressure and flow through all drift chambers is regulated by a system of valves and mass flow controllers, all under the supervision of an industrial programmed controller. A large fraction of the flow (80-90%) is recirculated through purifiers that remove oxygen and water vapour, but not nitrogen. In 1995, nitrogen from gas leaks in the drift chambers and from diffusion in the window foils accumulated in the loop to an equilibrium concentration of 1.1%. This influenced the drift velocity in the gas mixture and resulted in a gain reduction as confirmed by independent studies [12]. Work on the chamber gas leaks as well as decreasing the re-cycled fraction from 90% in 1995 to 80% in 1996 (20% exhaust), reduced the nitrogen contamination to a stable level of 0.4% with negligible influence on both drift velocity and gain.

The DC readout system consists of Amplifier/Shaper/Discriminator (ASD) cards mounted onboard the drift chambers, driving ECL signals on 30 m long flat cables to LeCroy 1877 Multihit FastBus

TDC's in the external electronics trailer. The design goal (especially in the case of the FC's and DVC's) was chamber operation at low gas gain ($\sim 10^4$) to maximize chamber lifetime and reduce particle flux dependence of the gas gain due to space charge effects. To combine this goal with good spatial resolution requires operation at low threshold – well below 10^5 electrons from the wire. This in turn requires both low loise performance of the amplifiers as well as great care in the radio-frequency design of the electronics enclosure on the chambers, to maintain electronic stability. All ground elements including the ASD cards themselves should be considered as radio-frequency resonators, and the lowest frequency of any resonant mode should be kept well above the pass-band of the amplifiers. For example, this dictates that the ground plane of each 16-channel ASD card continuously contact the electronics enclosure along both sides of the card via special high-conductivity card guides.

During the first year of operation in 1995, all drift chambers performed satisfactorily and alone provided the tracking data that were used in the physics analysis. As discussed later, performance was improved in 1996-97 by the addition of the DVC's.

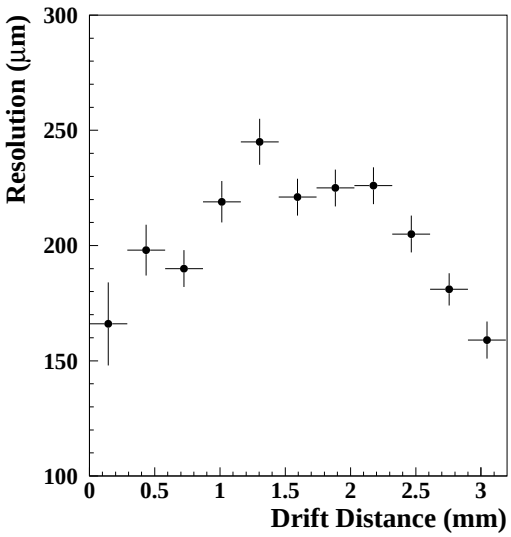

Figure 5: FC resolution as function of drift distance.

5.2.1 The Front Drift Chambers.

The front drift chambers FC1 and FC2 provide good spatial resolution immediately in front of the spectrometer magnet. Each chamber above or below the beam consists of one module of six sense planes; thus the total front drift chamber package presents twelve sense planes to a charged particle. Design parameters are listed in Table 1.

A drift cell size of only 7 mm (3.5 mm maximum drift length) was chosen to provide fine spatial granularity to maximize tolerance to both correlated and uncorrelated background. It emerged that uncorrelated background is mostly from collimator showers, at the average level of only 0.1 tracks per event. For a minor fraction of the events, the FC occupation from correlated tracks can be substantial, but is always acceptable.

The ASD design is similar to that of the LeCroy 2735DC card, except with a low-noise front end and pulse shaping added. With the input transistor (MMBR941LT1) used in common emitter mode with feedback, channel to channel gain variation is about $\pm 10\%$. In order to optimize pulse pair resolution and hence rate capability, pulse shaping between stages is also added. A long tail due to positive ions from the avalanche drifting to the cathodes is cancelled by shaping with two stages of pole-zero-cancelled differentiation. To facilitate testing of the chamber system, a linear monitor point is provided for each channel.

The threshold can be varied from approximately 0.07 to 1.25 μA at the input. At the lowest value, it will trigger efficiently on an impulse charge of approximately 12,000 electrons, resulting in 8 ns wide pulses at both the linear monitor and ECL logic outputs. An impulse charge of 1600 electrons produces a linear pulse of about the same magnitude as the RMS noise. In the 1995 running period, the FC threshold was dictated by ambient noise radiated by the target r.f. system. In 1996, the target r.f. noise was reduced and the electronics enclosure was improved, allowing a threshold of 140 nA from the wire, corresponding to a charge impulse of about 20,000 electrons. The power consumption per board is 0.3 A at +5 V and 0.55 A at −5.2 V, or 270 mW per channel. Hence moderate forced air cooling is provided.

Values of the resolution and efficiency of the chambers in 1996 are plotted as a function of track position across the drift cell in Figs. 5 and 6. The values shown for the resolution are the result of a fitting technique that removes the contribution of the tracking resolution to the track residuals. These values therefore better represent the resolution of the chambers.

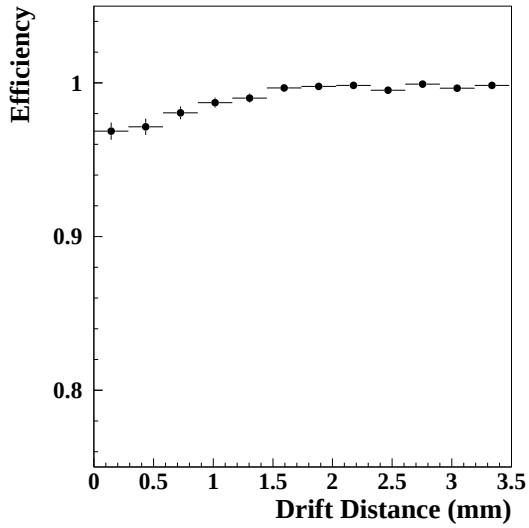

Figure 6: FC single-plane efficiency as function of drift distance.

5.2.2 The Back Chambers.

The back drift chambers BC1/2 and BC3/4 are in the size regime where special attention is required in the mechanical design to maintain the rigidity and stability necessary for uniform wire tension and precise alignment. These detectors are described in detail in [13]. The active areas of the modules were chosen according to their z-positions and the acceptance of the spectrometer. The geometrical parameters are listed in Table 1. Each module contains 14 fiberglass/epoxy (GFK) frames of 8 mm thickness, including 6 wire frames. They are clamped between two 38 mm thick non-magnetic stainless steel frames. The total thickness of a module is 190 mm. Because of their great length, the frames were prestressed to maintain the wire and foil tensions. The wires are located precisely by contact with accurate pins made of Polyoxymethylene with 5 μm tolerance, inserted in holes drilled in the GFK frames with a precision of better than 50 μm. The holes are located along a curved convex locus that compensates the expected stress deflection of the frames, in order to prevent displacement of the U and V wires. A mean deviation of 14 μm for the position of the holes was measured. Pins precisely located in holes can be produced much more easily than combs and allow convenient installation of the wires. The gas is injected directly into the wire gaps and exhausted via the window gaps. Work on the chamber gas leaks after the 1995 running period reduced the leak rate of the BC's to the level of diffusion through the window foils. The cathode wires and foils are operated at the same negative high voltage of typically 1770 V; the anode wires are at ground potential. More details on the BC mechanical construction can be found in [14] [15].

The chamber BC1 is located in the fringe field of the magnet. It has been verified by simulations using the program GARFIELD [16] that a vertical component of 0.1 T contributes to a deviation in the measured coordinate of < 60 μm, which can be neglected in the analysis.

The BC performance was studied extensively in test beam measurements illuminating essentially only one drift cell per plane. Under these conditions the HV/threshold setting 1750 V/50 mV was found to be the optimum working point, yielding $\sigma = 175$ μm resolution ($\sigma = 150$ μm in the central region of the BC drift cell) and 96.3% efficiency at 6% cross talk. The efficiency was determined from the occurrence of chamber signals in a rather narrow $\pm 4\,\sigma$ corridor around the reference track, which was defined by a silicon micro strip detector telescope [17, 18].

The BC performance was evaluated using production data from normal running. The widths of Gaussian fits to the central portions of the residual distribution for all tracks crossing the plane with an angle $< 1°$ is given in Fig. 7 as function of the drift distance for both BC1/2 and BC3/4. This plot was obtained by combining the data from all cells of all planes. Tracks close to the sense wire (i.e. small drift distances) are excluded because this data point is strongly affected by the difficulties in resolving the left/right ambiguity. However, a smooth behaviour of the residual can be assumed. As expected, the best value is measured in the central region of the drift cell. The results are approximately 210 μm for BC1/2 and 250 μm for BC3/4.

The average BC plane efficiency for electron and positron tracks is found to be well above 99% for 1996 data. The situation is somewhat worse for all tracks, which are mainly hadrons, due the smaller energy deposited in the chambers by hadrons. The plane efficiency drops to 97% when all tracks are considered. The efficiency is calculated by using the reconstructed track as a reference and adopting the same corridor width as used in the reconstruction program to find the hits belonging to a track, i.e. about $\pm 3\sigma$, where σ is the plane resolution. The dependence of the ef-

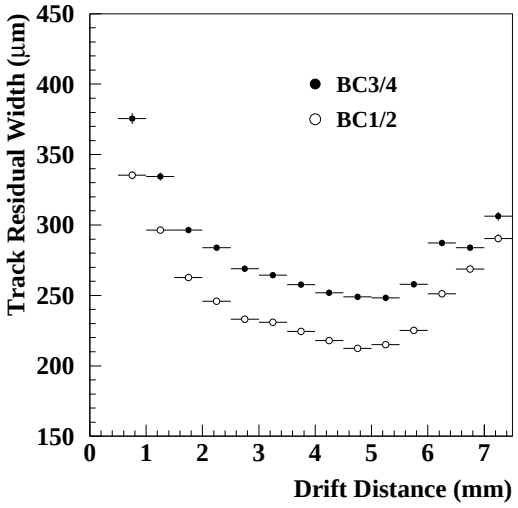

Figure 7: Width of the BC1/2 and BC3/4 residual distribution as function of the drift distance for tracks with an incident angle $< 1°$.

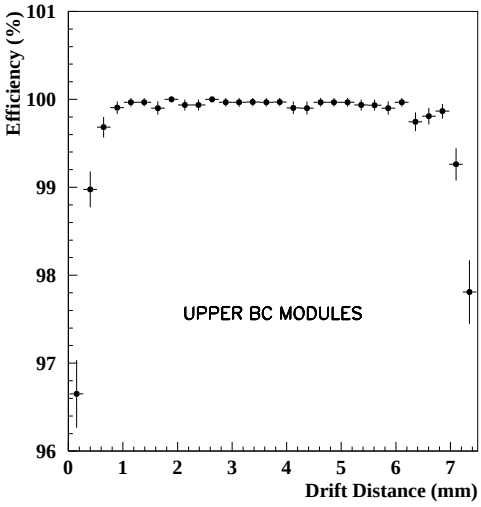

Figure 8: BC efficiency as a function of the drift distance for the upper BC modules under normal running conditions.

ficiency on the drift distance averaged over all drift cells is shown in Fig. 8.

Investigations of the long term stability of the 1995 data showed the expected correlation between chamber performance and atmospheric pressure, which led to varying working conditions.

A system to compensate for atmospheric pressure variations by dynamically adjusting the high voltage was introduced during the 1996 running period. A 'nominal' high voltage setting of 1770 V was chosen for an atmospheric pressure of 1013 mbar. The actual operating voltage was computed using a parametrisation of the gain versus atmospheric pressure given in Ref. [19]. The high voltage setting is corrected in steps of 1 Volt over a range of $\pm$ 20 Volts. This scheme significantly improves the stability of the chambers as can be seen in Fig. 9. The dependence of the average plane efficiency on the atmospheric pressure is presented for data before and after introduction of the gain stabilisation scheme in the middle of 1996 running. The overall improvement in efficiency using this system is 1 to 2 %. Threshold settings of 65 mV for the BC1/2 and 80 mV for the BC3/4 have been used.

The operation of the eight BC modules was remarkably stable and reliable in the first 2.5 years with low dark currents.

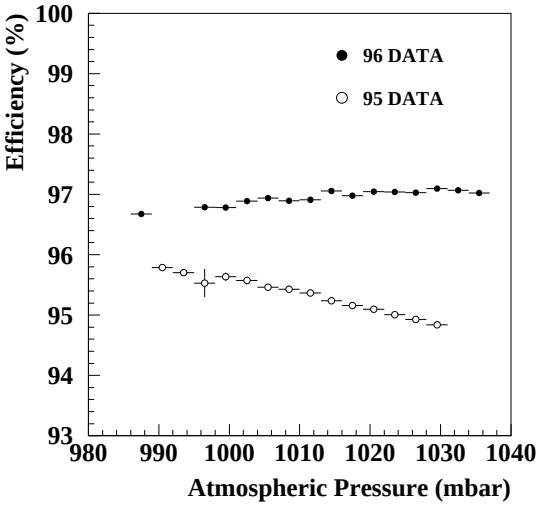

Figure 9: Averaged BC plane efficiency as function of the atmospheric pressure for the 1995 data sample (open circles) and a 1996 data sample after introducing a gain stabilisation scheme (filled circles). For details see the text.

5.3 The Drift Vertex Chambers

Notwithstanding the adequate performance of the tracking system during the 1995 commissioning year, redundancy in the front region was insufficient. Loss of a single FC plane could have had serious consequences. There was also foreseen the need for front tracking elements with larger acceptance for a future upgrade to provide muon detection beyond the standard acceptance. Hence an additional Drift Vertex Chamber (DVC) pair was constructed, and installed immediately following the VC's for use starting in the 1997 running period. The DVC drift cell design is similar to but slightly smaller than that of the FC's. However, the DVC acceptance extends vertically from ± 35 mrad to ± 270 mrad, and covers ± 200 mrad horizontally.

An acute design problem arising from the DVC location near the target chamber exit window is the close proximity of the active area to the beam pipe. This is solved in part by separating the functions of gas enclosure and chamber frames. The gas enclosure or box design is similar to that of the VC's, with a very thin wall less than 1 mm from the beam tube. Each of six wire planes in a box is clamped between its own pair of cathode foil planes. All planes can be installed together in the box while they are mated with the signal feed-throughs in the lid. However, the planes are thereafter precisely aligned by two pins equipped with gas seals, externally inserted through the box and all the planes. The ends of these pins provide external alignment fiducials. A gas injector is also externally inserted through the box wall into each anode plane after its installation in the box. The gas spills out of the active gaps into the box, and hence to a common exit port. Both the signal feed-throughs and the gas injectors are designed for mechanical accommodation sufficient to avoid constraining the alignment of the planes with respect to the box.

The readout system of the DVC's is identical to that of the FC's, resulting in similar performance in 1997 except for one of the twelve DVC planes, which suffered a broken wire immediately after installation.

5.4 The Magnet Chambers

The proportional wire chambers MC1 through MC3 located in the gap of the magnet were originally intended to help resolve multiple tracks in case of high multiplicity events. Since low backgrounds have made this unnecessary, their primary function is now the momentum analysis of relatively low energy particles, from the decay of Λ's for example. Since the MC's operate in a strong magnetic field and resolution of ± 1 mm is sufficient, multi-wire proportional chambers with digital single bit-per-wire readout were chosen. The magnet has a tapered pole configuration that implies a different size for each pair of chambers. The active areas of the three chambers given in Table 1 are dictated by the spectrometer acceptance together with magnetic dispersion at a nominal trigger threshold positron energy of 3.5 GeV.

Each chamber consists of three submodules U, X and V, laminated into one module with common gas volume. Each submodule consists of an anode plane at ground potential and two cathode planes with a common negative HV connection unique to this submodule, typically at 2850 V. The distance between anode and cathode planes is 4 ± 0.03 mm and the centers of neighbouring submodules are separated by 21 mm. The gas mixture has the same constituents as the drift chamber gas, but with proportions (Ar-CO_2-CF_4 65:30:5) optimized for MWPC operation (see Table 1).

The most difficult aspect of the MC design was the limited space inside the magnet for the frames and onboard electronics. The electronics are mounted on the front and back faces of the chambers in the barely adequate space between the magnet pole face and the spectrometer acceptance. Thin flexible printed circuit foils connect the wire frames to the electronics. The readout is the LeCroy PCOS IV system, including an on-chamber card design configured specifically for this application [20]. In addition to signal amplification, these cards provide discrimination and delay as well as latching in response to the event trigger. The high speed serial readout (up to 20 Mbit/s) greatly reduces the cabling in the very confined space of the magnet gap. The most severe constraint on MC operation is the inaccessibility of the detectors and the on-board electronics for the entire running period. It is not possible to work on the detectors during regular monthly accesses because they are buried inside the magnet. Unfortunately, a faulty batch of discriminator/latch chips together with a less-than-optimal design of the output motherboards used in 1995 created a reliability problem. The failure of a single chip that reads out only 8 wires disabled as many as 16 cards, corresponding to 256 wires. This process in combination with a Low Voltage distribution malfunction eventually resulted in the failure of a large fraction of the MC system, with overall track-

ing efficiency of only 45%. A redesigned motherboard eliminated this problem for 1996 operation. The MC system then performed reliably with typical efficiency per plane of 98-99%. Electronics failures in the 1996-97 running period resulted in the loss of only 0.5% of the channels (3 of 688 cards).

The very restricted air flow in combination with the power dissipation of 250 mW per channel makes water cooling a necessity. Flexible metallic fingers contact the tops of the SMD chips and conduct the heat to water-cooled plates between the cards. The water system operates at a pressure less than atmospheric to eliminate the danger of leaks.

The contribution to the spectrometer momentum resolution for 10 GeV positrons by Coulomb multiple scattering in the magnet chambers and air between FC2 and BC1/2 is $\theta_{rms} = 0.15$ mrad. (If the air were replaced by helium, it would be decreased to 0.11 mrad.) Thus the ratio of θ_{rms} to the magnet deflection angle is equal to 0.0024, independent of energy. This is small compared to other contributions.

5.5 Alignment

Errors in the relative alignment of the various elements of the tracking system are an important contribution to the resolution in reconstructed kinematic quantities. The initial alignment during detector installation was done using conventional optical techniques, but difficulties with optical access to the components limited the expected accuracy of this process to a few hundred micrometers in x and y, and of order 1 mm in z. It was always expected that the relative detector alignment would have to be improved in the data analysis through the study of track residuals with the spectrometer magnet turned off. This procedure was refined over the first three years of operation to the point that drift chamber alignment errors are no longer a major contribution to tracking resolution [21].

5.5.1 Laser Alignment System

It was considered essential to have a means to continuously monitor the relative alignment of the tracking detectors for two reasons. First, the detectors are mounted on a complex support system that is not simply interconnected so that its response to temperature changes and gradients is difficult to predict. Also, the front detectors are supported ultimately via the spectrometer magnet field clamp, which might suffer distortion from magnetic forces. Such an effect was detected with this monitoring system, and eliminated by stabilizing the clamp mount. Secondly, if a detector must be replaced with a spare after the laborious alignment analysis has been done, it is desirable to be able to avoid having to repeat this process immediately with new field-off data.

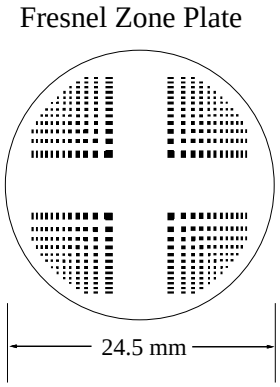

Figure 10: Fresnel zone plate made of 13 μm thick stainless steel with a diameter of 24.5 mm.

A solution to both of these problems is to have on each detector module optical targets that are continuously accessible to a remotely operated image recording system [22] . The type of system that was chosen employs two well-collimated parallel laser beams passing through the entire spectrometer in the beam plane, on either side of and parallel to the beam axis. The 2 cm diameter beams are created by one He-Ne laser and a semi-transparent mirror. Two optical target assemblies are mounted precisely and reproducibly on each detector element. Each assembly includes a remotely-controlled actuator that can move an optical target into the path of a laser beam, arriving at a precise and reproducible stop. Only one target is in a laser beam at a time. The type of target used – the Fresnel zone plate – is similar to that used in the SLAC accelerator alignment monitoring system. It is made by etching a precise pattern through a thin metal foil. This avoids any deflection of the beam from imperfections in the planarity of transparent material. A Fresnel zone plate is shown in Fig. 10. The large unperforated central regions were left for the sake of mechanical stability. They have the disadvantage that they produce secondary fringes in the images.

The zone plates on each detector are specified with a focal length equal to the optical path length from

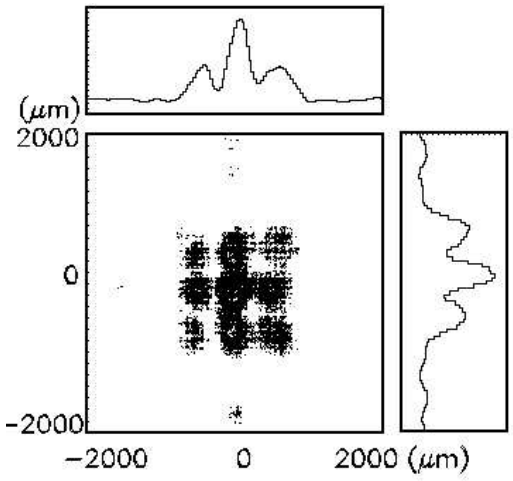

Figure 11: Typical Fresnel pattern image detected by the CCD camera. A one-dimensional projection is shown at the top and on the right. Nine peaks are visible at the center. The position of the central peak is fitted.

the target to the image recording component, which is a lensless CCD camera with a pixel size of 11 μm $\times$ 11 μm. Hence any shift in the detector or target is reproduced with unity magnification as a shift in the focal pattern at the camera. The camera image frames are digitized and recorded via a VME based system.

Since there are two targets on each detector at x=$\pm$45 cm, all transverse detector coordinates can be monitored. No absolute alignment is attempted with this system. In fact, long term stability of the laser beams is not assumed, since the optical paths contain several mirrors that are subject to instability. The beams must remain stable only for the 10 minute period required to cycle through all targets in each beam path. Only the relative x and y positions of the images recorded within that cycle are interpreted as being significant. Thermal wavering of the beams is reduced by insulating the beam path through the warm magnet shielding plate using a foam-cell tube. Several camera frames are averaged to minimize the effects of the wavering.

A Fresnel pattern image is shown in Fig. 11 . The FWHM of the central peak is about 300 μm. The precision of the laser alignment system is 30 - 50 μm.

5.6 Track Reconstruction

The HERMES reconstruction program (`HRC`) [23] is very efficient because it makes use of two unusual methods: the tree-search algorithm for fast track finding and a look-up table for fast momentum determination of the tracks. The full reconstruction of 30 Monte Carlo events on an SGI R4400 processor takes only one second.

5.6.1 The Fast Pattern Recognition Algorithm

The main task of the reconstruction program is to identify particle tracks using the hits in the tracking chambers. Each detector plane gives spatial information in one coordinate, and only by combining the information of many detectors is it possible to reconstruct the tracks uniquely in space. There are several track-finding algorithms in common use. `HRC` uses the tree-search algorithm, which turns out to be very fast. This algorithm is implemented in the following way:

As a first step, "partial" tracks have to be found in projections, separately in the region in front of and behind the spectrometer magnet. The track projections are approximately straight lines in those regions, except for small curvatures caused by the magnetic fringe fields, and kinks coming from secondary interactions and straggling.

The basic idea of pattern recognition using the tree-search algorithm is to look at the whole hit pattern of the detectors with variable (increasing) resolution as illustrated in Fig. 12. At each step of the iteration the entire partial track is seen. However only at the end is the full detector resolution reached. The detector resolution is roughly 250 μm and the active width of a chamber is of the order of a few meters. Therefore after about 14 steps in the binary tree, the resolution of the detector of $\sim 1:2^{14}$ would be reached. For the purpose of track finding (not fitting) a resolution of $1:2^{11}$ is sufficient, which reduces the maximum number of iterations in the `HRC` tree-search to about 11.

In each step of the iteration, the algorithm checks if the pattern (at the given resolution) contains a sub-pattern that is consistent with an allowed track. Fig. 13 shows examples of allowed and forbidden patterns. All allowed patterns are generated and stored in a data base at the initialisation phase of the program. The comparison is very fast as only look-up

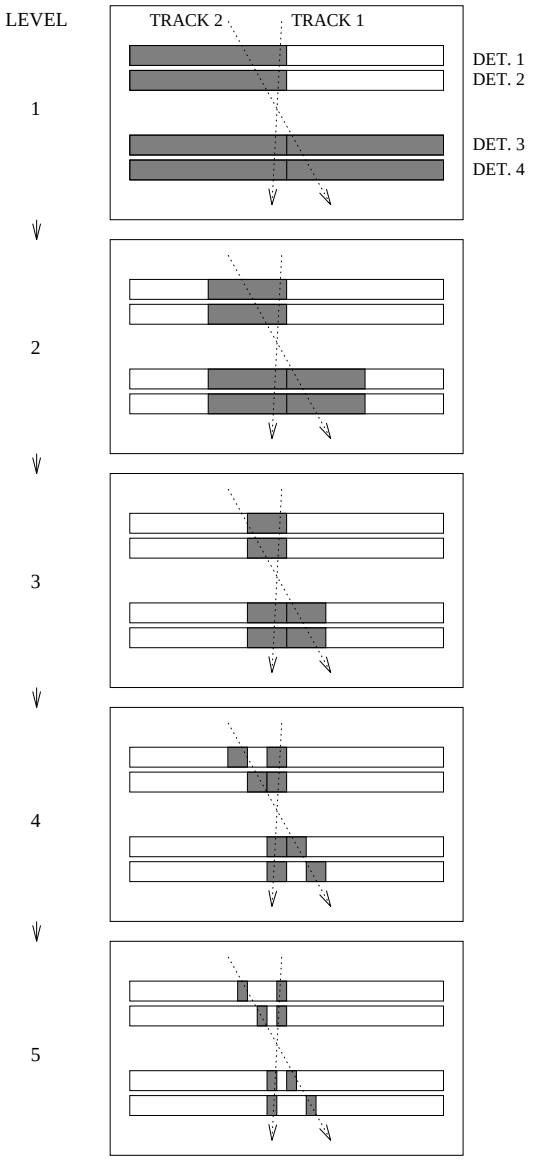

Figure 12: The tree search algorithm looks at the hits of the tracking detectors with artificially reduced resolution. In every tree search level the resolution is doubled until a resolution is reached that is optimal for track finding.

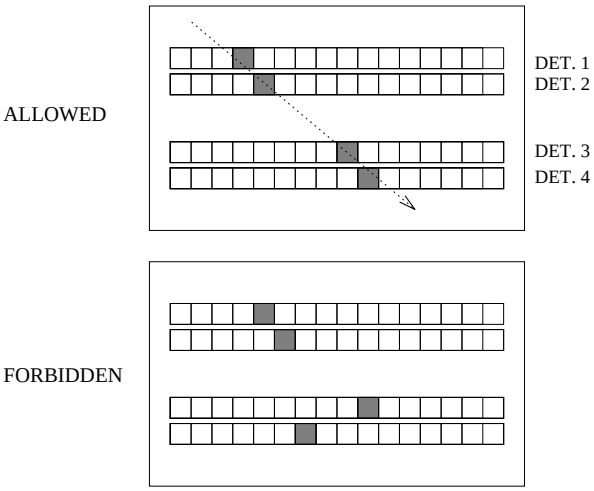

Figure 13: At each tree search level, the allowed and forbidden patterns are well defined. The program compares the measured pattern with the data base and determines if the measured pattern is consistent with an allowed track.

tables are used; no calculations have to be done during event processing.

The number of allowed track patterns at the full resolution is of the order of 10^8. Without optimization, this large number would make the algorithm useless for two reasons: memory space problems to store all the patterns, and CPU time problems to compare with each of them. The following methods avoid these problems:

- If one compares the allowed patterns from one iteration to those from the following one (called parent and child in the following) it becomes obvious that only a very limited number of children exist for each parent. At initialisation time all links between the allowed patterns of each generation are calculated, i.e. all children for each parent are stored in the data base. The number of comparisons now becomes small: if a pattern is recognised at one generation, only its children have to be checked in the next generation. The number of children for each parent is typically 4 to 8. This solves the CPU problem.

- Symmetry considerations can be used to reduce the number of patterns that have to be stored. If two patterns are mirror symmetric, or if they are identical except for a transverse shift, they are stored as one pattern. Most important is that if

a child is identical to a parent, then the child is linked to the parent and all grand children become identical to the children. This simplification is based on the fact that we are looking only for approximately straight tracks. This reduces the number of branches in the tree-search significantly. The number of patterns in the data base is of the order of 50,000, which is small compared to the original number of 10^8.

After applying the tree search algorithm to the U and V planes, the partial tracks in these projections are defined. They are called tree-lines. By testing all combinations of tree-lines and merging them with hits in the x coordinate, the partial tracks in space are found. The tree-search algorithm is not applied to the x-coordinate directly as portions of the X-planes of the VC chambers are tilted and thus do not fulfil the symmetry conditions. However, the x projections are used for track finding in the back region.

The procedure described until now is applied independently to the front and back regions, resulting in a set of front partial tracks and another set of back partial tracks. All combinations of front and back partial tracks are tested to see if they match spatially within a specified tolerance at the x-y plane in the center of the magnet. Those combinations that match are combined to form a full track, after refitting the track geometry to the chamber hits, subject to the match condition. The matching condition is refined by various small corrections depending on partial track geometry and deflection angle from the first iteration.

5.6.2 The Fast Momentum Look-Up

As a second feature in `HRC`, a very fast method has been developed to determine the momentum of a track, which is given by the deflection in the inhomogeneous field of the spectrometer magnet. Tracking through a magnetic field is very CPU intensive. The new method makes obsolete the tracking through the magnetic field on a track by track basis. Instead, a large look-up table is generated only once during initilization. It contains the momentum of a given track as a function of the track parameters in front of and behind the magnet. The relevant track parameters are the position and the slope of the track in front of the magnet and the horizontal slope behind the magnet. The resolution of the table has been chosen such that, using interpolation methods, the contribution by `HRC` to the precision of the track momentum determination is better than $\Delta p/p = 0.5\%$. The look-up table contains 520,000 numbers. This method of momentum determination is extremely efficient.

The vertical slope and position of the track behind the magnet are not kinematically relevant degrees of freedom and are used only to determine the track quality and reduce the number of ghost tracks. They are not used in the determination of the kinematic parameters, as the resolution and alignment of the VC-FC system is superior to the resolution of the back chambers.

5.6.3 Tracking in 1995 without VC's and DVC's

As mentioned earlier, the VC performance in 1995 was not optimal due to difficulties in production of the APC readout chips. The performance of the substitute prototype chips resulted in marginal efficiencies (60-90%) and many "hot" channels. The DVC's were conceived later and became available only for 1997. Hence an alternative track reconstruction method was developed using only the drift chamber data. The back partial tracks are generated as usual and the front partial tracks are generated using only the FC data. The front-back matching search is done as usual, except with somewhat larger tolerances. Then, for all matching pairs of partial tracks, the match point at the centre of the magnet defined by the back partial track is used to refine the front partial track by pivoting it about a conserved space point midway between FC1 and FC2. Thus the front partial track is forced to agree at the magnet midpoint with the presumably higher quality information from the back partial track. This process was used successfully for the 1995/96 physics analysis, with approximately a factor of two loss of resolution in kinematic quantities relative to what could be expected if the VC's were fully operational.

5.7 Tracking System Performance

The performance of the tracking system has been studied using the detailed HERMES Monte Carlo (HMC) simulation of the experiment, which is based on the GEANT [24] software package. Resolutions for several quantities were estimated by performing a Gaussian fit to spectra of the difference between the generated and reconstructed quantities. Results for the measured quantities p (momentum) and θ (scattering angle) are shown in Figs. 14, 15. The mo-

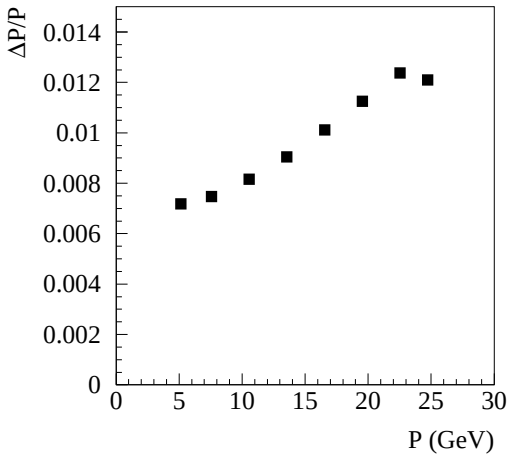

Figure 14: Momentum resolution in the HERMES spectrometer, deduced from Monte Carlo studies.

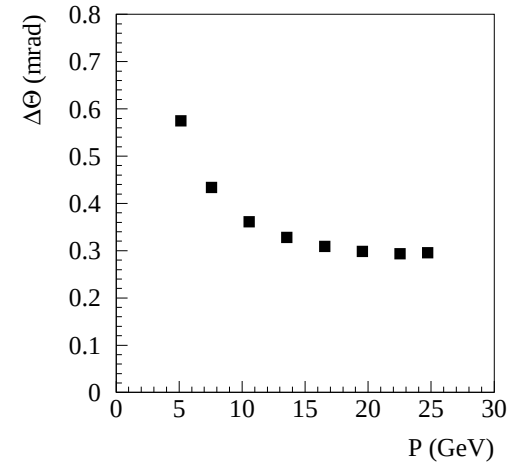

Figure 15: Resolution in scattering angle deduced from Monte Carlo studies.

mentum resolution is 0.7-1.25% over the kinematic range of the experiment, while the uncertainty in the scattering angle is below 0.6 mrad everywhere. Bremsstrahlung in materials in the positron path cause the momentum resolution function to have a standard deviation considerably larger than that of the fitted Gaussian. The resolutions for x and the square of the momentum transfer are shown in Figs. 16, 17. The x resolution varies from 4% to 8% while the Q^2 resolution is better than 2% over most of the kinematic range.

Finally, the absolute calibration of the spectrometer can be checked using the decay of K_S mesons into two pions. The invariant two-pion mass is plotted in Fig. 18. The reconstructed K_S mass agrees to one part per mil with the value of the Particle Data Group [25] (497.4 MeV vs 497.7 MeV). The width of the peak (σ= 0.0057, or $\approx$1.1%) agrees with the resolution determined by Monte Carlo methods.

5.8 Kinematic Variables

Numerous measured and calculated quantities have been compared to the Monte Carlo simulation of the experiment (HMC). Fig. 19 shows some of these comparisons for the momentum p of the scattered particles, the variable x defined earlier, the four-momentum transfer squared (Q^2), and the square of the photon-nucleon invariant mass (W^2). The normalisations of the histograms are arbitrary. The points represent data while the shaded histograms are the Monte Carlo simulation. The agreement is good over most of the range of the variables.

The kinematic plane for the experiment (Q^2 vs ν) is shown in Fig. 20. The typical DIS acceptance is defined by the following software cuts shown as the bold lines on the plot:
- Scattering angle: 40 mrad $< \theta <$ 220 mrad;
- Fractional energy transfer: y= ν/E < 0.85;
- $W^2 > 4$ GeV^2;
- $Q^2 > 1$ GeV^2.

6 The Particle Identification Detectors

6.1 General Description

The HERMES particle identification system discriminates between positrons, pions, and other hadrons. It provides a factor of at least ten in hadron suppres-

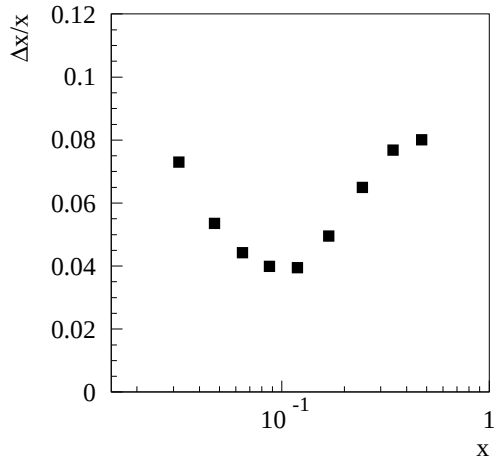

Figure 16: Resolution for the Bjorken x variable, deduced from Monte Carlo studies.

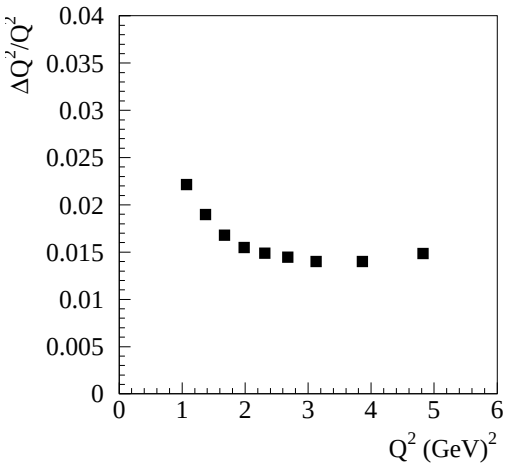

Figure 17: Resolution for the square of the four-momentum transfer, Q^2, deduced from Monte Carlo studies.

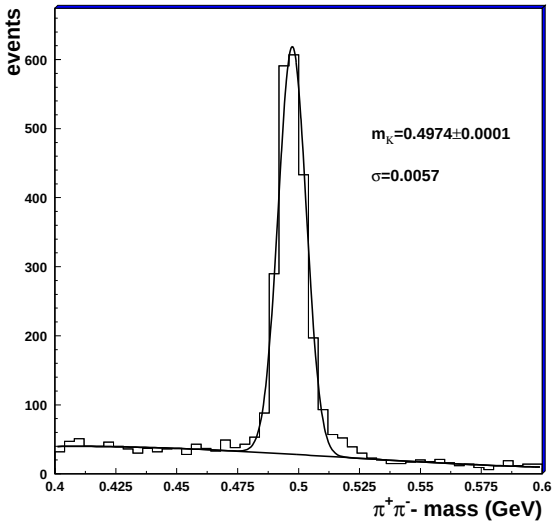

Figure 18: Invariant mass of $\pi^+ - \pi^-$ pairs. The reconstructed K_S mass agrees very well with the PDG value.

sion at the DIS trigger level to keep data acquisition rates reasonable. The rate of DIS positrons is much exceeded by that of hadrons from photoproduction by a factor as high as 400:1 in certain kinematic regions. The system provides a hadron rejection factor (HRF) of at least 10^4 in offline analysis to keep the contamination of the positron sample by hadrons below 1% for the whole kinematic range. The HRF is defined as the total number of hadrons in the spectrometer acceptance divided by the number of hadrons misidentified as positrons. It depends on the selected efficiency of positron identification (see Table 3 later for typical efficiencies and contaminations). Since most of the hadrons are pions, we will often refer to a pion rejection factor (PRF). The PID system also discriminates pions from other hadrons for the important semi-inclusive measurements that will allow the contribution of the valence and sea quarks to the nucleon spin to be isolated.

The PID system consists of four sub-systems: a lead-glass calorimeter, two plastic scintillator hodoscopes, one of which is preceded by two radiation lengths of lead and which acts as a pre-shower detector, a transition radiation detector, and a threshold Čerenkov detector (see Fig. 1). The calorimeter and the hodoscopes are used in the first level trigger to select DIS events. Beam tests at CERN have shown that this combination gives a HRF of several thousand for an electron efficiency of 95% in offline analysis. The rejection factor is estimated to be ap-

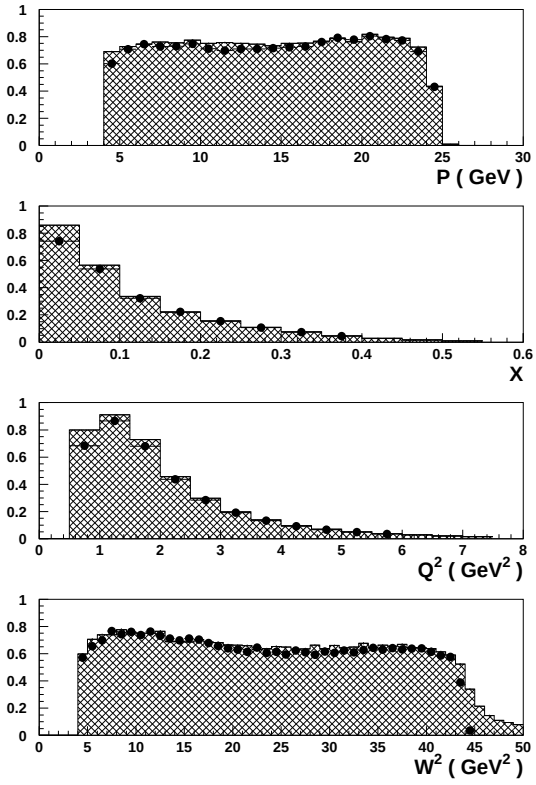

Figure 19: Kinematic variables p, x, Q^2, and W^2. The points are data while the shaded histogram is a Monte Carlo simulation. The normalisations of the histograms are arbitrary.

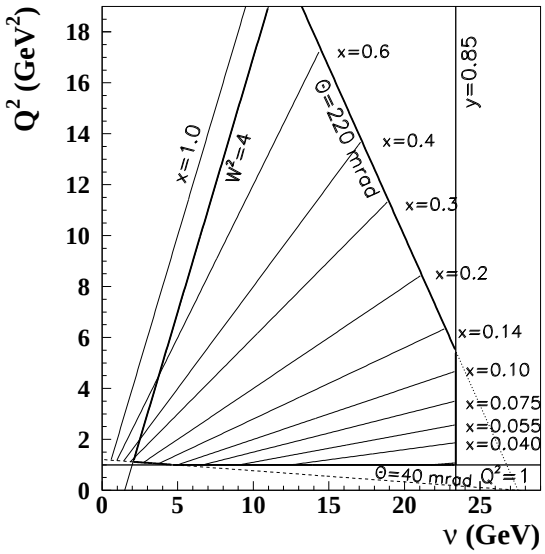

Figure 20: Kinematic plane for the HERMES experiment. See text for details.

proximately 10 in the trigger. The TRD consists of 6 modules in each half and provides an additional HRF of over 100 for 90% e^+ efficiency (several hundred if a probability based analysis is used). The main function of the threshold Čerenkov detector is to distinguish pions from other hadrons for the semi-inclusive measurements. In future, kaons will also be identified using a ring imaging Čerenkov detector (RICH). An upgrade of the current threshold detector to a RICH is being prepared for 1998. Each sub-system is described in detail in the following sections.

6.2 The Calorimeter

The function of the calorimeter is to provide a first level trigger for scattered positrons, based on energy deposition in a localized spatial region ($\geq$3.5 GeV in 1995 and the beginning of 1996 and $\geq$1.4 GeV in late 1996 and 1997); to suppress pions by a factor of $\geq$10 at the first level trigger and $\geq$100 in the off-line analysis; to measure the energy of positrons and also of photons from radiative processes or from π^0 and η decays.

The solution chosen to meet these requirements consists of radiation resistant F101 lead-glass blocks [26] arranged in two walls of 420 blocks each above and below the beam. The properties of F101 glass are listed in Table 2.

Chemical composition (weight %)	
Pb_3O_4	51.2
SiO_2	41.5
K_2O	7.0
Ce	0.2
Radiation Length (cm)	2.78
Density (g/cm^3)	3.86
Critical Energy (MeV)	17.97
Molière radius (cm)	3.28
Refractive Index	1.65
Thermal Expansion coefficient (C^{-1})	8.5 x 10^{-6}

Table 2: Properties of F101 Glass.

Each block is viewed from the rear by a photomultiplier tube (PMT). The blocks have an area of 9×9 cm^2, a length of 50 cm (about 18 radiation lengths), and are stacked in a 42×10 array. The blocks were polished, wrapped with 0.051 mm thick aluminized mylar foil, and covered with a 0.127 mm thick tedlar foil to provide light isolation. Each block is coupled to a 7.62 cm Philips XP3461 PMT by a silicone glue (SILGARD 184) with refractive index 1.41. A μ-metal magnetic shield surrounds the PMT. A surrounding aluminum tube houses the μ-metal and provides the light seal. It is fixed to a flange that is glued to the surface of the lead glass. This flange is made of titanium, matching the thermal expansion coefficient of F101.

To prevent radiation damage of the lead glass, both calorimeter walls are moved away vertically from the beam pipe by 50 cm for beam injection. The monitoring of gain and ageing is achieved using a dye laser at 500 nm, which sends light pulses of various intensities through glass fibres to every PMT of the calorimeter, and additionally to a reference counter photodiode. The various intensities are produced by a rotating wheel with several attenuation plates. The light is split in several stages before being fed into the glass fibres. As the gain of the photodiode is stable, the ratio of the PMT amplitude to that of the photodiode signal can be used to monitor relative gain changes in the photomultipliers. Over three years of operation, there has been no observed degradation of performance that would suggest ageing effects.

Radiation damage to the lead-glass is also monitored indirectly using TF1 [27] blocks placed behind the calorimeter. This material is much more sensitive to radiation damage than F101. Therefore, a degradation of the response would be seen much sooner in these monitor detectors if there were a large radiation dose incident on the back of the calorimeter caused by showers produced by beam loss in the proton machine. So far no variation has been observed in their response, indicating that the effect of radiation damage is negligible.

Measurements with 1-30 GeV electron beams were performed at CERN and DESY with a 3×3 array of counters. Each lead-glass block was also calibrated within ≈1% at DESY in a 3 GeV electron beam incident at the center of the block.

The performance of a 3×3 array of counters showed [28]: *i*) an energy response to electrons linear within 1%, over the energy range 1-30 GeV; *ii*) an energy resolution that can be parameterized as $\sigma(E)/E\ [\%] = (5.1 \pm 1.1)/\sqrt{E\,[GeV]} + (1.5 \pm 0.5)$: this is similar to that obtained for other large lead-glass calorimeters; *iii*) a spatial resolution of the impact point of about 0.7 cm (σ); *iv*) a PRF of $\approx (2.5 \pm 1.2) \cdot 10^3$ integrated over all energies in combination with the preshower detector, for a 95% electron detection efficiency.

The central values of E/p distributions for positrons, measured for tracks incident on each block during the 1995 data taking period are plotted in Fig. 21. E and p are respectively the energy of positrons measured by the calorimeter and the momentum determined by the spectrometer. The ratio has a central value of 1.00 with a width (σ) of 0.01, demonstrating that the response of the counters is uniform to ≈ 1%. The long term stability of the detector response of 1% is determined from the mean value of the E/p distribution, measured for each run for the counters nearest to the beam. This value also includes the contribution of the radiation damage produced in one year of operation, indicating the effect of the radiation damage is negligible.

The overall calibration of the calorimeter can be determined by the reconstruction of π^0 decays. Fig. 22 shows the π^0 invariant mass for events with two γ clusters. The centroid of the peak for the 1995 data is (134.9±0.2) MeV with a σ= (12.5±0.2) MeV in good agreement with the particle data group value [25]. The calorimeter is described in more detail in a separate paper [29].

6.3 The Hodoscopes

A scintillator hodoscope (H1) and Pb-scintillator preshower counter (H2) provide trigger signals and

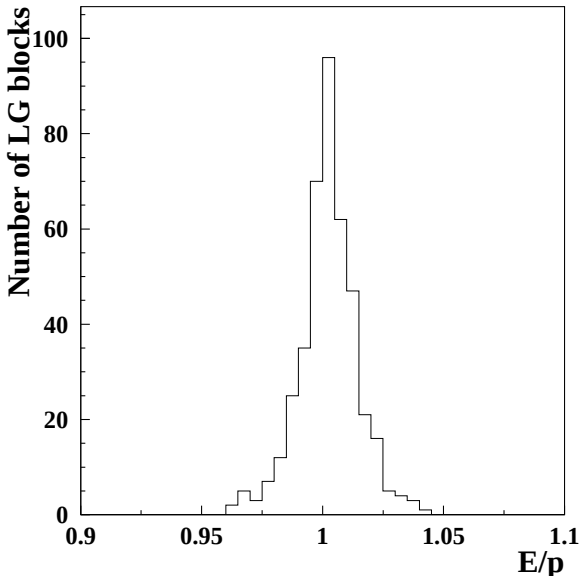

Figure 21: Central values of the E/p distribution for each block (one entry each) measured for positrons for data collected during the first year of operation.

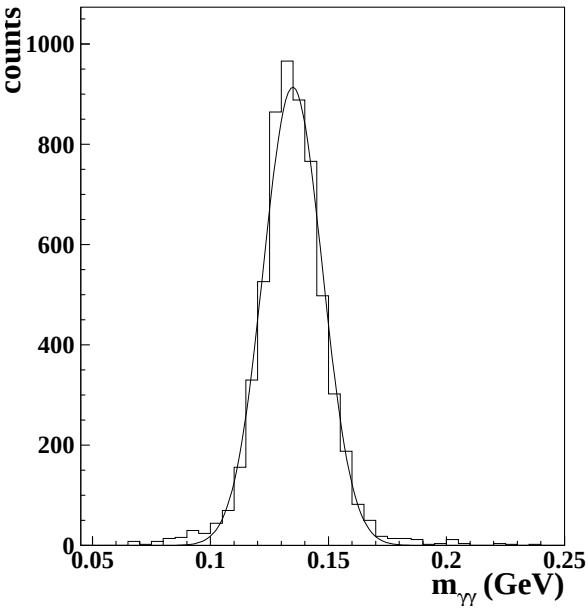

Figure 22: π^0 mass reconstructed from 2 γ cluster events.

particle identification information. Both counters are composed of vertical scintillator modules (42 each in the upper and lower detectors), which are 1 cm thick and 9.3 cm x 91 cm in area. The material for the modules is BC-412 from Bicron Co., a fast scintillator with large attenuation length (300 - 400 cm). The scintillation light is detected by 5.2 cm diameter Thorn EMI 9954 photomultiplier tubes, one coupled via a light guide to the outside end of each scintillator (away from the beam plane). The modules are staggered to provide maximum efficiency with 2 - 3 mm of overlap between each unit.

In addition to providing a fast signal that is combined with the calorimeter and H1 to form the first level trigger (H0 was implemented in 1996; see below), the H2 counter provides important discrimination between positrons and hadrons. This is accomplished with a passive radiator that initiates electromagnetic showers that deposit typically much more energy in the scintillator than minimum ionizing particles. The passive radiator consists of 11 mm (2 radiations lengths) of Pb, sandwiched between two 1.3 mm stainless steel sheets. The response of the H2 counter to positrons and hadrons is shown in Fig. 23. While pions deposit only about 2 MeV, positrons produce a broad distribution of deposited energies with a mean of 20 - 40 MeV that depends weakly on the energy of the incident positron. A PRF of $\sim$ 10 is possible with 95% efficiency for positron detection.

6.4 Forward Trigger Scintillators

In 1995, a large number of showers generated by the proton beam were able to satisfy the trigger requirements for DIS positrons. There were typically between 20 and 100 triggers per second of this type, compared to about 35 positron triggers and 35 pion-induced triggers per second (with the standard ^{3}He target operation and about 30 mA of positron current).

A forward trigger scintillator (H0) placed directly upstream of the front drift chambers was introduced in 1996 to eliminate these triggers by distinguishing forward and backward going particles using the time of flight between the front and rear scintillators.

The total time required for a light-speed particle to traverse all trigger detectors is on the order of 18 ns, and hence a backward-going particle produces a pulse in the front counter that is displaced in time by about 36 ns from the normal trigger condition. Such a large time displacement allows for easy elimination of these

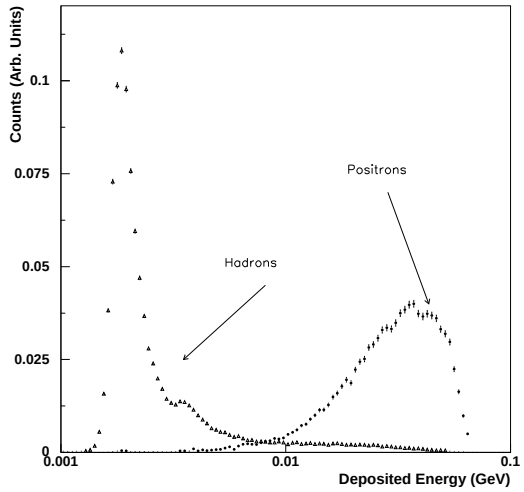

Figure 23: Response of the pre-shower detector to hadrons and positrons.

background events in the trigger.

The front trigger detectors consist of a single sheet of standard plastic scintillator, 3.2 mm thick (0.7% of a radiation length). The occupancy of the scintillators is such that segmentation of the detector is not necessary. The rate in each paddle is about 10^6 per second. The scintillation light is collected along the edge farthest from the beam axis into two sets of lucite strips and then into two 5.08 cm Thorn EMI 9954SB phototubes.

6.5 The Čerenkov Detector

Pion identification is provided by a pair of single-gas radiator threshold Čerenkov counters, one each above and below the beam. The units are located between the back drift chamber groups, BC1/2 and BC3/4. The radiator is a gas mixture at atmospheric pressure of nitrogen and perfluorobutane, C_4F_{10}, the composition of which can be varied to control the momentum interval over which pions can be distinguished unambiguously from other hadrons. The depth of the radiator volume is 1.17 m. During the first year of operation, the radiator was pure nitrogen for which the Čerenkov momentum thresholds for pions, kaons, and protons are 5.6, 19.8, and 37.6 GeV, respectively. In 1996-97, a mixture of 70% nitrogen and 30% perfluorobutane was used, which gives corresponding thresholds of 3.8, 13.6, and 25.8 GeV.

The body of each unit is constructed of aluminum. The entrance and exit windows have areas 0.46 m $\times$ 1.88 m and 0.59 m $\times$ 2.57 m, respectively. Each window consists of a composite foil of 100 μm of mylar and 30 μm of tedlar separated by a 1 cm gas gap from a second identical composite foil. Dry nitrogen gas continuously flowing through this gap in each window provides a barrier against the diffusion of atmospheric gas through the windows into the radiator gas volume. An array of 20 spherical mirrors (radius of curvature: 156 cm) mounted at the rear of the counter on Rohacell forms focuses the Čerenkov light emitted along particle trajectories onto corresponding members of an array of phototubes. The mirrors are coated with aluminum and magnesium fluoride and have a measured reflectivity of 90% at 400 nm. The mirror array is mounted with individual adjustment on a plane of 3.0 cm Rohacell foam reinforced with fibre glass epoxy films. The average effective particle path length in the gas viewed by the mirrors is 0.95 m.

The phototubes (Burle 8854) have 12.7 cm diameter photocathodes, and are fitted with Hinterberger-Winston light cones to maximize the light collection. The funnels have an entrance diameter of 21.7 cm and can accept light at angles of up to 26 degrees from the optical axis. They are coated with aluminium to give a reflectivity of 85% at 400 nm. Magnetic shielding for the phototubes is provided by three concentric μ-metal shields and a soft iron housing. The photocathode faces are coated with a layer of 200 μgm/cm^2 of p-Terphenyl and a protective coating of magnesium fluoride. This wavelength shifter increases the photoelectron yield [30]. The mean number of photoelectrons for a β=1 particle with a pure nitrogen radiator was measured to be slightly less than 3. LEDs mounted on each Winston cone provide an on-line gain monitoring system. Calibration spectra are accumulated during normal running with the LED amplitudes set sufficiently low so that strong single-photoelectron peaks are resolved cleanly. These peaks provide an accurate measure of the gain per photoelectron for each channel.

The typical response of the Čerenkov detector is shown in Fig.24. The single photoelectron peak is prominent and reasonably well separated from the pedestal.

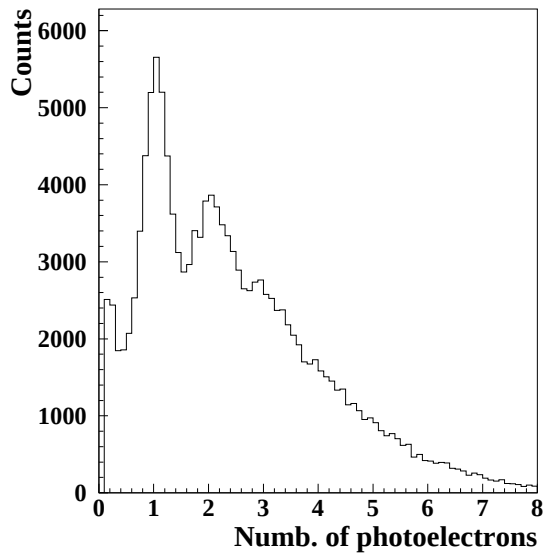

Figure 24: Response of the Čerenkov detector from 1995 data; note that events below 0.15 photoelectrons have been suppressed.

6.6 The Transition Radiation Detector

The purpose of the transition radiation detector (TRD) is to provide a pion rejection factor of at least 100 for 90% positron efficiency at 5 GeV and above.

Only positrons produce transition radiation in the HERMES energy regime and the detection of one or more TR X-rays in coincidence with the charged particle can be used to discriminate between positrons and hadrons. The X-ray is difficult to distinguish because it is emitted at an angle of $1/\gamma$ to the momentum of the charged particle and is therefore not separable in the detector from the positron.

Because the space restrictions imposed on the TRD were not severe, a relatively simple and economical design was chosen. Rather than optimize each module of the TRD for maximum performance, the overall performance is assured by the addition of extra modules. The design of the TRD was optimized using a Monte Carlo program that tracks charged particles and photons down to an energy of 1 keV. Care was taken to model properly the production of δ-rays in the radiator and the detector gas as well as hadronic showers in the radiator. Elements of the TRD simulation were later integrated into the general spectrometer simulation [31].

The HERMES TRD consists of 6 modules above and below the beam. Each module contains a radiator and a Xe/CH_4 filled proportional chamber. In addition, there are two flush gaps on either side of each detector through which CO_2 is flowed to reduce the diffusion of oxygen and nitrogen into the chamber. Such contaminants would affect the response significantly. CO_2 is used in the flush gaps because it is easily removed from the chamber gas during recirculation.

The use of polyethylene foils as a radiator is not practical for HERMES because of the large size of the modules (active area: 325 x 75 cm^2). It is not possible to maintain a uniform separation of the foils for such a large radiator. A good approximation to a foil radiator is provided by a pseudo-random but predominantly two-dimensional matrix of fibers [32]. Several radiators were compared in a test beam at CERN: foils, fiber matrices with different fiber diameters, and polyethylene foams. Fiber radiators were shown to produce a response only slightly less than that from a foil radiator. The final design uses fibers of 17-20 μm diameter in a material with a density of 0.059 g/cm^3. This density is significantly less than would be found to be optimal if hadronic showers and delta rays from the radiator were ignored. The radiators are 6.35 cm thick, which corresponds to an average of 267 dielectric layers.

The detectors are proportional wire chambers of conventional design, each of which consists of 256 vertical wires of 75 μm gold coated Be-Cu separated by 1.27 cm. The wires are not soldered but rather held in crimped pins. This makes it much simpler to replace a broken wire in situ. The wires are positioned with 25 μm accuracy using precisely machined holes for the crimp pins in plastic strips (Ultem) that are glued to the aluminium chamber frames. The chambers are 2.54 cm thick. Xe/CH_4 (90:10) is used as the detector gas because of its efficient X-ray absorption. The electric field in the chamber is produced by a +3100 V potential applied to the anode wires; the cathode foils are at ground potential. The large voltage on the anode wires is needed to produce an electric field in the critical region between the wires of sufficient strength to collect the ionization electrons within the 1 μsec ADC gate used in the readout electronics. The wire diameter was chosen to be unusually large to allow operation at this high voltage while limiting the gas gain to about 10^4. The drift cell properties were optimized using the computer program GARFIELD [16].

The active gas volume of the detector is defined by the cathodes which are 50 μm thick mylar foils aluminized on both sides. The foils are stretched to an unusually high tension (1.75 kN/m) to make them more stable against pressure differences between the detector and the flush gaps. This is important because a 10 μm deviation in the position of the cathode causes a 1% gain shift in the detector. All frames supporting the anode wires and the cathode foils were pre-stressed during construction.

The tension of each wire was measured using resonant vibration induced by the combination of a current flowing through the wire and an external magnetic field. Furthermore, each wire was scanned with an X-ray source every 2.54 cm during operational tests after assembly. Any gain variations of more than 10% caused by imperfections in the wire resulted in the wire being removed and re-strung.

The signals from the wires are amplified by electronics mounted along the long edge of the detector furthest from the beam. Balanced differential signals are transmitted over 35 m long twist/flat cables to the electronics trailer. The use of differential signals reduces common mode noise, which would severely degrade TRD performance. Receiver modules filter, amplify, and delay the signals by 256 ns while a first level trigger decision is made, at which time they are digitized by LeCroy 1881M Fastbus ADC's. Test pulses are injected via an antenna at the other end of the wires to allow for a quick check of the detector and readout electronics without beam.

Since Xe is expensive, the chamber gas must be recirculated and purified. Impurities in the gas are kept at acceptable levels by molecular sieves and activated copper ($N_2 \approx 1\%$, $CO_2 \approx 0.25\%$, $O_2 \approx$ ppm). As a further precaution to keep impurities low, all detectors were He leak checked during construction. This was particularly important to identify and plug leaks in the crimped pins used to fix the wires. A sophisticated pressure control system based on an industrial programmed controller adjusts the flows into the detector and the gaps in such a way that the differential pressure between these volumes is less than a few μbar [33]. A pressure stability of 1-2 μbar corresponds to a gain stability of a few percent. The chambers track atmospheric pressure in order to avoid using very thick foils to contain the gas. However, experience has shown that even during periods of large atmospheric pressure variations, the differential pressure between the detector volume and the flush gaps is maintained below 1-2 μbar by the control system.

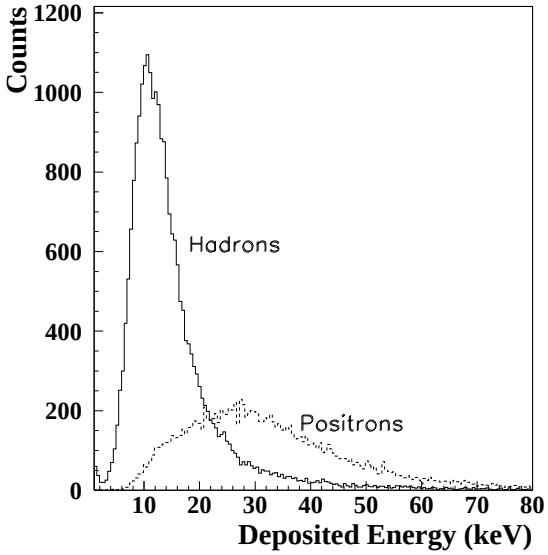

Figure 25: Response of a single TRD module to positrons and hadrons, integrated over all momenta. Data from 1995 were used for this plot.

The gas system is described in more detail in [33].

Both positrons and hadrons deposit energy in the detector due to the ionisation of the chamber gas (dE/dx). The most probable energy deposited by a 5 GeV pion is about 11 keV. Positrons deposit on average approximately twice this amount of energy due to transition radiation and the relativistic rise in dE/dx. The response to positrons and hadrons in one module is shown in Fig. 25. Pure positron and hadron samples are selected by placing stringent, inefficient conditions on the other PID detector responses. The distributions are very broad and it is clear that information from several modules must be combined for high quality hadron rejection. In particular the long, high energy tail in the hadron distribution overlaps significantly with the positron distribution. A simple but effective method of analysis is the truncated mean method. In this technique, the largest signal from the six modules is discarded and the average of the remaining five modules is used. This procedure reduces the mean of the positron distribution but has a much more significant effect on the hadron tail that is due to rare events - production of energetic knock-on electrons. Fig. 26 shows the truncated mean distributions for the HERMES TRD derived from 1995 data. It is clear that the separa-

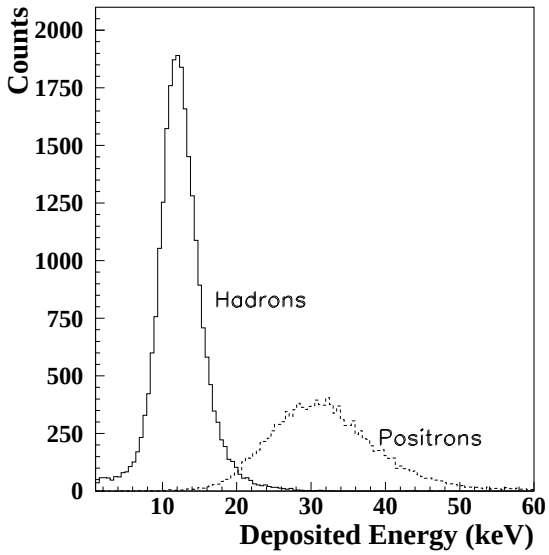

Figure 26: Truncated mean for six modules for positrons and hadrons, integrated over all momenta. Data from 1995 were used for this plot.

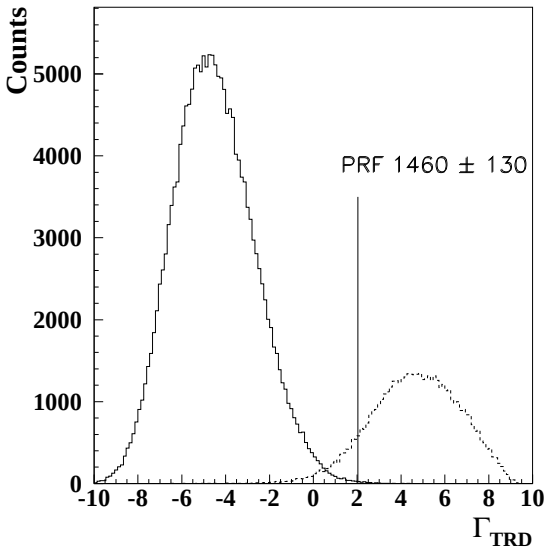

Figure 27: The logarithmic likelyhood Γ_{TRD}, integrated over all momenta, for hadrons (positrons) is plotted as the solid line (dashed line). Data from 1996 were used for this plot. The vertical line indicates the location of a 90% efficiency positron cut.

tion of the hadrons and positrons is greatly enhanced. The pion rejection factor varies with energy because both the energy loss by charged particles and the production of transition radiation depend on the energy of the incident particle. It is customary when describing the performance of a TRD to place a cut on the response of the detector such that 90% of the positrons are above the cut. The cut is set for higher efficiency for physics analysis. Using the truncated mean method, the energy-averaged PRF is about 150 for 90% positron efficiency. If the data are analysed as a function of momentum, a PRF of 130 is deduced at 5 GeV, exceeding the design goal. The PRF is somewhat smaller for lower momenta (80 at 4 GeV) and larger for higher energies (up to 150).

The PRF can be improved using a probability based analysis similar to the one described in the section on PID system performance below. A probability function can be defined as

$$\Gamma_{TRD} = \log_{10}[P_{e+}/P_h],$$

where P_{e+} and P_h are the probabilities that a particle was a positron or a hadron respectively. The result of such an analysis for 1996 data is shown in Fig.27. A cut for 90% positron efficiency results in a PRF of 1460 $\pm$ 130. Even at 95% positron efficiency, the PRF remains very good (489$\pm$25).

6.7 PID System Performance

The responses of the four PID detectors are combined to provide good hadron rejection. This has been done in several ways. The simplest technique is to consider the responses individually, determine a cut that separates positrons and hadrons in each detector, and define a positron/hadron as a particle identified as such in all detectors. A very clean sample of a given particle type can be produced in this way but at the cost of efficiency. Typically, this technique is used only for detector studies. The efficiency of the system can be improved while retaining good particle type separation by using a probability based analysis. The responses of the calorimeter, the pre-shower detector, and the Čerenkov detector are combined to produce the quantity PID3 defined as

$$\text{PID3} = \log_{10}\left[(P^e_{Cal}P^e_{Pre}P^e_{Cer})/(P^h_{Cal}P^h_{Pre}P^h_{Cer})\right],$$

where P^i_j is the probability that a particle of type i produced a given response in detector j. The P^i_j's are determined by comparing the detector responses for each track to typical response functions for each detector called parent distributions. The latter are either derived from the data or modelled using Monte

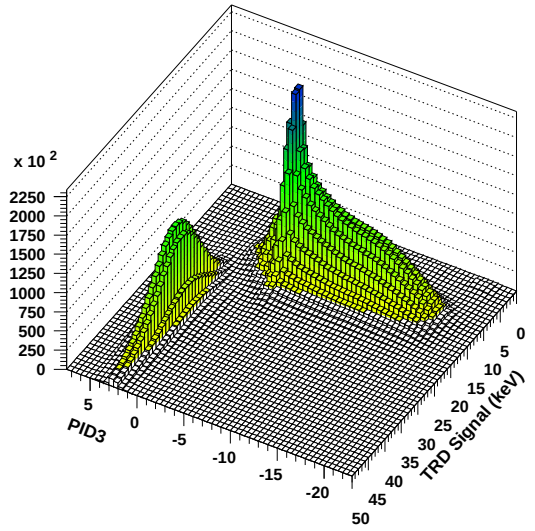

Figure 28: Plot of the PID3-TRD plane. Positrons appear at positive PID3 and large values of 'TRD Signal'.

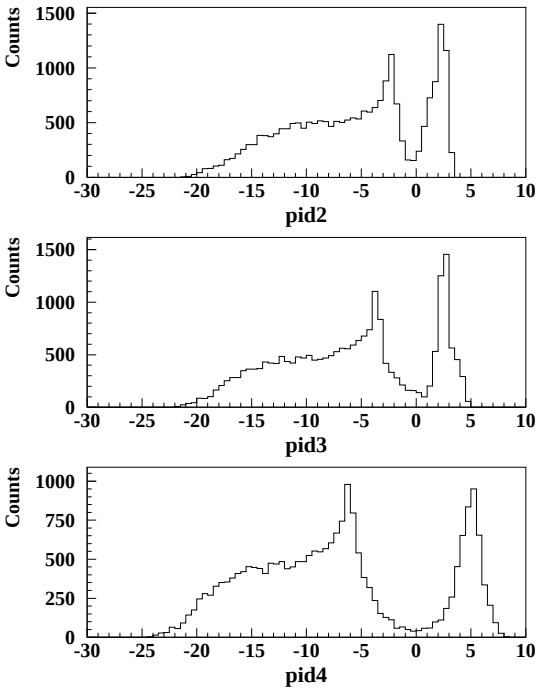

Figure 29: Comparison between the PID parameters PID2, PID3 and PID4 for the 1995 data set. Positrons have positive values of PID2, PID3, and PID4, while hadrons have negative values for these quantities.

Carlo techniques. The use of momentum dependent parent distributions is required to account for the varying responses of the detectors. PID2 is defined in a similar way to PID3 using only the calorimeter and the pre-shower detector. PID4 including the TRD is also defined but will be discussed later.

For the 1995 data, PID3 was used in combination with the TRD truncated mean to make a two-dimensional cut identifying positrons and hadrons. This is shown in Fig. 28 where it is clear that a clean positron sample can be isolated at positive PID3 and large TRD truncated mean (TRD Signal). The advantage of using this technique rather than combining all four detectors is that it allows detailed systematic studies to be done on the probability analysis [34]. For example stringent cuts (low efficiency, but high purity) can be applied to the TRD to define clean samples of positrons and hadrons that can be used to study the PID3 response and vice-versa.

One can incorporate the TRD into the probability analysis to improve performance even further. The resulting function is labelled PID4. However, one then loses the straightforward systematic cross-checks described above and Monte Carlo simulation must be used to estimate the contamination of each particle sample as well as the detection efficiency. A graphical comparison of PID2, PID3, and PID4 is shown in Fig. 29. In order to keep as many events as possible for the final analysis, a so-called PID downshifting scheme was implemented. If all PID detectors provide valid data, a cut on a 2-dimensional PID3-TRD plot is used, which is equivalent to a straight cut on PID4. However, if information from either the TRD or the Čerenkov detector is not available a more limited scheme is used: if the TRD data are not available PID3 is used, while if the Čerenkov data are not useful a two-dimensional cut on the PID2-TRD plane is considered. For the analysis of the inclusive data in 1995, the full PID3-TRD scheme was used for over 97% of the useful events.

The hadron contamination of the positron sample was determined in several ways. In the more limited PID schemes, a value can be derived from clean particle samples obtained using the detector not considered in that particular method. However, for the full PID scheme, the hadron contamination can only be estimated due to the fact that all detectors are used in the analysis and there is no control detector to define clean samples. The different analysis techniques give consistent results. The most straightforward of these methods is a simple fit to the total probability distributions using an assumed shape for the tail for

each particle sample in the overlap region, for example a Gaussian or an exponential. The values of the hadron contamination for a given positron efficiency are listed in Table 3 for the x bins used in the analysis of the 1995 data. More details on the particle identification system can be found in ref. [34].

x-Bin	PID3-TRD	
	e^+ eff.	h^+ cont.
0.023 - 0.04	97.77	1.18
0.04 - 0.055	98.38	0.81
0.055 - 0.075	98.78	0.55
0.075 - 0.1	99.21	0.37
0.1 - 0.14	99.44	0.22
0.14 - 0.2	99.64	0.16
0.2 - 0.3	99.71	0.16
0.3 - 0.4	99.72	0.16
0.4 - 0.6	99.72	0.11

Table 3: Positron Efficiency and Hadron Contamination in % for the PID3-TRD Method (1995).

Time of flight information from the hodoscopes can be used to separate pions, kaons, protons, and deuterons at low momentum (up to ≈2 GeV). The time of flight is referenced to the accelerator bunch signal. The TDC values must be corrected for vertical position in the scintillators to take into account the transmission time of the light. The time resolution is 300 ps. Fig. 30 shows the time of flight as a function of momentum. Protons, deuterons and perhaps some kaons are visible.

Another very effective way to do particle identification is to reconstruct the mass of particles with decay products in the spectrometer. This has been done for π^0, ρ, η, K_S, ϕ, ω, J/Ψ, and Λ. More details on decaying particles can be found in ref. [35].

7 The Luminosity Monitor

The luminosity measurement is based on the elastic scattering of beam positrons from target gas electrons $e^+e^- \to e^+e^-$ (Bhabha scattering) and the annihilation into photon pairs $e^+e^- \to \gamma\gamma$. The cross sections are known precisely, including radiative corrections, e.g. $e^+e^- \to e^+e^-\gamma$, $e^+e^- \to \gamma\gamma\gamma$ [36]. In the future with an electron beam in HERA, the process $e^-e^- \to e^-e^-$ (Møller scattering) will be used [37]. The scattered particles exit the beam pipe at z = 7.2 m and are detected in coincidence by two small calorimeters with a horizontal acceptance of 4.6 to 8.9 mrad, which is limited by the size of the beam aperture in the magnet shielding plate. For a beam energy of 27.5 GeV the symmetric scattering angle is 6.1 mrad and both scattered particles have half of the beam energy.

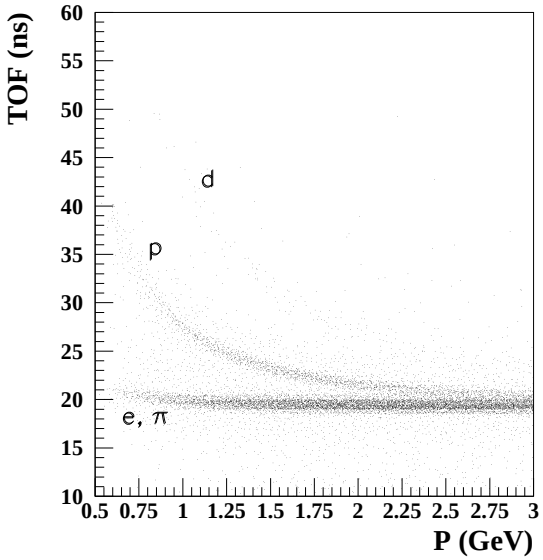

Figure 30: Time of flight vs momentum for hodoscope H1.

Density ρ (g/cm^3)	7.57
Radiation length X_0 (cm)	1.03
Molière radius R_M (cm)	2.38
Critical energy E_C (MeV)	9.75
Index of refraction n	2.15
Optical transparency (nm)	≥ 380
Radiation hardness (Gy)	$7 \cdot 10^5$

Table 4: Properties of $NaBi(WO_4)_2$ crystals.

Due to the high radiation background in the region very near to the beam, the calorimeter consists of Čerenkov crystals of $NaBi(WO_4)_2$ [38, 39, 40], which have a very high radiation hardness on the order of $7 \cdot 10^5$ Gy. To further minimize radiation damage, the calorimeters are moved away from the beam pipe exit window by ∼ 20 cm in the horizontal direction for beam injection and dumping. The properties of $NaBi(WO_4)_2$ are summarized in Table 4. The small radiation length and the small Molière radius allow a very compact calorimeter design. Each calorime-

ter consists of 12 crystals of size 22×22×200 mm^3 in a 3×4 array. The crystals are wrapped in aluminized mylar foil and coupled with optical grease to 1.9 cm Hamamatsu R4125Q photomultipliers with a radiation hard synthetic silica window and a bialkali photocathode. For monitoring the gain of the counters, each crystal is fed with light pulses from an optical fibre of the HERMES gain monitoring system described in section 6.2. An energy resolution of $\sigma(E)/E \simeq (9.3\pm0.1)\% / \sqrt{(E)}$ (E in GeV) has been determined for a 3×3 matrix from test beam measurements with 1-6 GeV electrons.

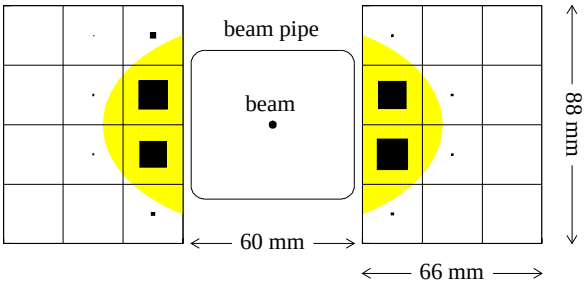

Figure 31: Hit distribution in the calorimeters of the luminosity monitor. The size of the boxes is proportional to the number of hits per channel. The shaded area shows the beam pipe acceptance.

Fig. 31 shows the hit distribution in the calorimeters. Most of the scattered particles hit the inner crystals near the beam pipe. The deposited energy is reduced by lateral shower leakage, especially for hits near the inner crystal edge. A scatter plot of the energy in the left detector versus the energy in the right detector is shown in Fig. 32. Most of the background events have a high energy deposition in only one of the detectors while Bhabha events have a high energy deposition in both detectors. They are separated from background by triggering on a coincident signal with energy above 5 GeV in both the left and right calorimeter. A Bhabha coincidence rate of 132 Hz was measured with this trigger scheme for a beam current of 20 mA and a ^{3}He areal target density of $1 \cdot 10^{15}$ nucleons/cm^2. This provides a statistical accuracy of the luminosity measurement of 1%, within about 100 s.

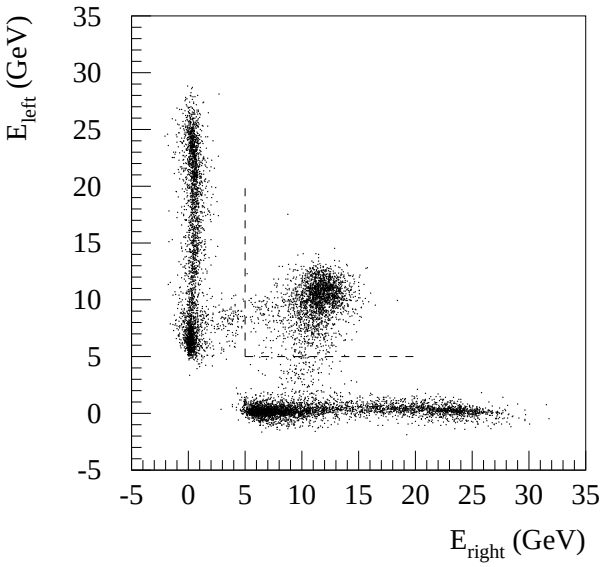

Figure 32: Scatter plot of the deposited energy in the left luminosity detector versus the deposited energy in the right detector. The dashed line shows the trigger threshold of 5 GeV in both detectors for Bhabha events.

8 The Trigger

8.1 Trigger Requirements

The function of the trigger system is to distinguish interesting events from background with high efficiency, and initiate digitization and readout of the detector signals. HERMES requires physics triggers corresponding to deep-inelastic positron scattering, photoproduction processes (where no positron is detected) and additional triggers for detector monitoring and calibration. The trigger hierarchy is potentially capable of four levels. However, for running in 1995-97 only the first-level trigger was required.

The first-level trigger decision is made within about 400 ns of the event using prompt signals of the scintillator hodoscopes, the calorimeter, and a few wire chambers. This can be divided into the time necessary for signal formation in the detectors and transportation to the electronics trailer (≈ 250 ns including the transit time of the particle from the target), and the time needed for a decision by the trigger electronics (≈ 150 ns). The first-level trigger initiates digitization by the readout electronics. The

second-level trigger could use any information available within the 50 μs during which time a hardware clear of the Fastbus readout electronics is possible. The third-level decision could be made on a timescale of a few hundred micro-seconds by existing digital signal processors in Fastbus, which would first read out only that part of the detector information required for the decision. In fourth level, the full data stream could be filtered by a farm of Intel Pentium Pro processors that can make a decision on a timescale of $\leq$1 ms. Only the first-level trigger is described below.

The DIS trigger selects positron events by requiring hits in the three scintillator hodoscopes, H0, H1, and H2, (only H1 and H2 in 1995) together with sufficient energy deposited in two adjacent columns of the calorimeter, in coincidence with the accelerator bunch signal (HERA Clock). The forward H0 scintillator was installed in 1996 because backward-going particles from the HERA proton beam are not adequately suppressed by the H1 – H2 timing alone. With H0 included, the primary sources of background are hadrons either produced from positron beam interactions in the upstream collimators, or photoproduced in the target. The requirement of hits in the H0 and H1 hodoscopes suppresses neutral particle background. The primary charged background discrimination is done using a calorimeter threshold set above the minimum ionizing energy deposition of 0.8 GeV. The calorimeter has high efficiency for electromagnetic showers, but relatively low efficiency for hadronic showers. The hodoscope thresholds were set below minimum ionizing. A calorimeter threshold setting of 3.5 GeV (used for the 1995 running and corresponding to $y \leq 0.85$) suppresses the charged hadronic background rate by a factor of ≥ 10 in the trigger. The typical trigger rate at a luminosity of 5×10^{32} nucleons/cm^2/sec, was about 50 Hz in 1995. The threshold was lowered to 1.4 GeV during 1996 to increase the y range to $y \leq 0.95$ and improve the acceptance for semi-inclusive particles.

The photoproduction trigger detects hadrons such as K, ρ, D^0, J/ψ and Λ^0 that are produced at low Q^2 and decay to two or more charged particles. Typically the scattered positron angle is too small for detection. The trigger requires charged particle tracks in both the top and bottom detectors, as identified by the three hodoscopes and the BC1 chamber as well as the HERA Clock. The back chamber requirement eliminates those showers originating in the upstream collimators, which are confined near the beampipe and hit the tips of the hodoscopes but not the wire chambers which are well shielded by the magnet steel.

8.2 First-level Trigger Architecture

The signals needed for the first-level triggers are the hodoscopes (H0, H1, H2), a multiplicity of two or more hits in the back wire chambers (BC1), and a cluster of calorimeter blocks with total energy above threshold. Hits in the top AND bottom halves of the spectrometer are required for the photoproduction trigger.

Each hodoscope photomultiplier (PMT) signal is passively split with one output going to a LeCroy 1881M analog to digital convertor (ADC) and the other going to a LeCroy 3420 Constant Fraction Disciminator (CFD). The individual CFD outputs are fed to LeCroy 1875A time to digital convertors (TDC). The high impedance OR outputs of the CFD's for each hodoscope wall are connected together in a chain to form the hodoscope logic signals.

Each calorimeter wall consists of 42 columns of 10 lead-glass blocks each. PMT signals from each block in a given 10-block column are split to provide ADC inputs, and added linearly to form a Column Sum using custom-built NIM modules. Segment Sums of 20 blocks are formed by linear addition of pairs of adjacent Column Sums, in LeCroy 428F modules. At least one Segment Sum contains more than 95% of the energy of each electromagnetic shower. All combinations of adjacent columns are used to fully cover a calorimeter wall. The analog Segment Sum signals are discriminated by CFD's to form TDC and logic signals.

The back chamber signals are used only for the photoproduction trigger. ECL signals are utilized from each of the 256 wires of the top and bottom X-planes of BC1. LeCroy 4564 modules are used to produce logical OR's of adjacent wires in groups of 16. The multiplicity of 16-wire groups that fired is determined in a LeCroy 4532 module.

The resulting ECL logic signals are reshaped by a LeCroy 4415A differential discriminator and collected into a signal bus. Relative delay adjustments can be made with a LeCroy 4518 programmable CAMAC logic delay module. The trigger logic is established in LeCroy 4508 programmable logic units (PLU), which allow changes to be made easily. The signal bus provides the inputs to the PLU, which is strobed with the HERA clock. The PLU ECL outputs are converted to NIM, prescaled appropriately with CERN

prescalers, and brought together in the Master Event OR. The Master Event is retimed by the HERA Clock and gated by the data acquisition NOT BUSY signal to produce the Master Trigger that initiates digitization and readout of the event.

8.3 Trigger Performance

The purity of the deep inelastic scattering (DIS) trigger is good for a high calorimeter threshold (3.5 GeV) and acceptable for a low threshold (1.4 GeV). For a 3.5 GeV calorimeter threshold, two thirds of the triggers had tracks, 95% of reconstructed tracks came from the target, and one third had accompanying positrons. For a 1.4 GeV calorimeter threshold, the physics trigger rate increased by a factor of about 6 while the fraction of DIS positrons only went up by about 10%. These runs had significant contamination coming from the collimator just upstream of the target. About two thirds of the events had tracks, but only 70% of the tracks came from the target, with most of the remaining coming from the collimator.

Approximately one third of the photoproduction triggers have reconstructable tracks. Of these, over 3/4 have two or more tracks, due to the requirement of hits in the lower and upper part of the detector simultaneously. Only 6-7% have positrons, which is not surprising given that the aim of the trigger is to detect events at low Q^2 where the positron goes down the beampipe. However, most of the tracks come from the target region.

During normal polarised running with the high calorimeter threshold, 15% of the photo-production triggers were also DIS triggers. Roughly 2.5 photoproduction triggers were collected for each DIS trigger. During polarised running with the low calorimeter threshold the overlap increased to 40% due in part to the increased rate in the high-y DIS triggers. The number of photo-production triggers remained the same, since the calorimeter is not in this trigger.

9 Data Acquisition and Readout Electronics

The backbone of the data aquisition system is constructed in Fastbus. It consists of 10 front-end crates, the event collector crate, and the event receiver crate connected to the online workstation cluster via 2 SCSI interfaces. CERN Host Interfaces (CHI) act as Fastbus masters. To enhance their readout performance they are equipped in most places with Struck Fastbus Readout Engines (FRE), featuring one or two Motorola 96002 DSPs. The event collector in the electronics trailer is connected to the event receiver crate in a computer room via a Fibre Optical Link (STR330/FOL) plugged into the respective CHIs. Pairs of Fastbus crates, read via only one CHI/FRE, are formed by cluster interconnects (CI), where overall readout timing considerations allow for it. The drift chamber signals are digitized using LeCroy multi-hit multi-event 16 bit 1877 sparsifying multiblock 96 channel TDCs with a resolution of 0.5 ns/channel. Charge from the various photomultiplier tubes and the TRD is digitized by LeCroy multi-event 64 channel 1881M multiblock ADCs. The resolution is 50 fC/channel and the full scale range is 13 bits above pedestal. During a multiblock transfer from 1881M ADCs or 1877 TDCs, the CHI/FRE combination results in a readout time of 127 ns/word (CHI without FRE: 270 ns/word), where the slave timing is contributing 90 ns/word and the FRE 37 ns/word. The multiblock passing time (time for two neighbouring modules to pass the token) is found to be 640 ns. Reading beyond a cluster interconnect adds a penalty of about 50 ns/word. This results in a block read speed of more than 30 MB/s in crates having a master and more than 20 MB/s in crates beyond a CI. As soon as first data are collected into the FRE's input FIFO, the active DSP starts processing the incoming data, writing the output to its output FIFO. The LeCroy multi-event 10 bit 64 channel 1875A was choosen for digitizing the time of flight signals. The resolution is set to 25 or 50 ps/channel depending on the detector. As only six 1875A's are read out in total, the lack of multiblock capability on this unit is only a minor disadvantage. The magnet chamber readout is instrumented with the LeCroy VME based PCOS4 system, consisting of one 2749 and twelve 2748 modules. The readout time (including the transfer to the event collector memory) is 450 ns/hit wire. Vertex chamber data arrive from the detector as a 16 bit ECL STR330/ECL data stream, one 16 bit word containing the plane and strip number of one hit strip. Incoming data are passed in direct mode from the Struck ECL interface to the associated DSPs, where hot channels are suppressed using a linear 16 bit lookup table. The trigger pattern is available to all front ends, to allow for selective readout. Event collection is done from each FRE output FIFO via a cable segment, connecting directly to the FRE cable port. Double buffering is implemented in

all essential places to provide a low front-end deadtime. Event collection is done in parallel with the next event readout with incoming events processed alternately between two DSPs in each of the FREs. A typical overall reduction in event size from ≈18 to 10 KB/event is achieved at the DSP level.

In addition to the standard detector readout, there is implemented a variety of asynchronous independent events, capable of trigger rates exceeding 5 kHz, including the luminosity monitor and various high speed calibration and monitoring equipment. Depending on the application, the data from these events are either collected by the event collector during idle time or by dedicated additional CHIs and FREs. They can be defined either as so-called user events, or as a set of histograms read directly from CHI RAM or FRE DSP BRAM where they have been accumulated.

One VME branch with 4 crates and three CAMAC branches with a total of 9 crates are connected to the event builder crate to handle special data acquisition tasks, such as obtaining the electron bunch number, and slow control. The VME interface is a CHI/VSB2 module and VDB. The VME crates are connected via a STR723 in combination with a STR725. The CAMAC crates are controlled by standard CCA2 type crate controllers. Scaler information is obtained from STR200 32 channel 32 bit Fastbus scalers.

The code for both the 68030 and the 96002 is written in assembly language. An online library of Standard Fastbus, CAMAC and VME procedures for jobs that are not time-critical can be called from FORTRAN or C in the workstation cluster. These procedures are executed in the respective front-end CHIs. All event data and the slow control information are available for online monitoring and analysis in the online data stream, and are easily available to code in high level languages.

Data are written to 9 GB staging disks over the course of a fill of the storage rings, typically lasting 8-12 hours. The data are copied between fills to storage silos on the DESY main site via a FDDI link and associated hardware. In parallel, they are stored on local Exabyte tape drives for redundancy. The local system was switched to DLT tapes late in 1996. A total of 2 TB was recorded in 1995 and 4.1 TB in 1996. The deadtime during standard running is typically well below 10% and the downtime due to the data aquisition system is estimated to be below 1%. The possible throughput of 1.5 MB/s was determined by the CPU and I/O bandwidth of the event distributing work station (Alpha 3000X), which corresponds to a 150 Hz event rate at the average event size. By replacing the 175 MHz 3000X with a 266 MHz 5/266, this was doubled for 1997.

10 Beam Diagnostics and Tuning

Since HERMES is a fixed target experiment, the scattered particles are mostly forward and the detectors are necessarily in close proximity to the beamline. This makes the experiment sensitive to beam induced background. The two main sources of background associated with the positron beam are synchrotron radiation and showers from halo particles striking the collimators just upstream of the target. Several closed orbit corrections (i.e. that affect the beam only locally) are available to help minimize background. These are of two types: symmetric which affect the position of the beam at the interaction point (IP), and asymmetric which vary the angle at the IP. It was determined to be crucial to tune the beam in the straight section upstream of the experiment to minimize synchrotron radiation. In particular, background from this source is acceptable only when a special asymmetric orbit correction well upstream of the IP is optimized. The detectors most susceptable to backgrounds are the front tracking chambers and the TRD, the former because they must operate in front of the magnet and hence in the presence of a large flux of low energy particles, the latter because it is particularly sensitive to photons by design. The TRD was made less vulnerable to synchrotron radiation by adding a thin sheet of lead ($\ll$1 mm) in front of the first chamber to absorb some of the low energy incident photon flux.

To help optimize background conditions before the detectors are turned on, dedicated scintillators were installed around the beam pipe. This system is called the Tuning Scintillation Telescope (TST). The TST consists of 2 sets of scintillators (8 each) that are located upstream of the front chambers at z = +1.4 m and behind the luminosity detector at z = +8.3 m. Each set has two layers of 4 scintillators surrounding the beampipe to view the beam halo. The first layer is unshielded and therefore is sensitive to synchrotron radiation as well as charged particles. The second layer is shielded with 3 mm of lead, so the synchrotron radiation is mostly suppressed. Charged particle halo and synchrotron radiation can be identi-

fied using coincidences and anticoincidences between the first and second layers of scintillators. Beam tuning is then a matter of minimizing the counting rates and making them symmetric. The TST is used primarily during initial beam tuning when the accelerators are first turned on at the start of a running period, and at the beginning of a fill of the storage rings.

Beam position monitors (BPM) on either side of the IP allow the beam to be adjusted to a predetermined position and angle in a short time. The BPMs are particularly useful at the beginning of a fill of the storage rings.

The experiment is also exposed to particles that come from showers originating from the proton beam. A set of scintillators was installed around the proton beam pipe just behind the calorimeter to monitor this background. Background from this source varies significantly from fill to fill and even during a fill. However, essentially none of it is correlated with the events of interest so its main effect is to increase the trigger rate and decrease the proportion of good events going to tape. As outlined previously, the addition of the front trigger hodoscope (H0) has significantly improved the situation.

11 Summary

This paper describes the spectrometer built to measure the products of deep inelastic scattering of polarised positrons from polarised internal gas targets at HERA. After a relatively short commissioning phase, the experiment started recording data in 1995. All essential detectors have performed well with only a few component failures over the first two and a half years of running. The acceptance of the spectrometer allows the detection of hadrons in coincidence with the scattered positron. These important semi-inclusive measurements with the identification of pions and kaons are unique to HERMES and will allow the determination of the spin dependent quark distribution functions.

12 Acknowledgements

The HERMES collaboration would like to thank all those who participated in the design and construction of the spectrometer. We are particularly indebted to the MEA staff at DESY, many more of whom contributed than are mentioned in the author list. We also gratefully acknowledge the DESY management for its support.

This project has been supported by the FWO-Flanders, Belgium; the Natural Sciences and Engineering Council of Canada; the Dutch Foundation for Fundamenteel Onderzoek der Materie (FOM); the German Bundesministerium für Bildung, Wissenschaft, Forschung und Technologie; the German Academic Exchange Service (DAAD); the Italian Istituto Nazionale di Fisica Nucleare (INFN); Monbusho International Scientific Research Program, JSPS, and Toray Science Foundation of Japan; the United Kingdom Particle Physics and Astronomy Research Council; the U.S. Department of Energy and National Science Foundation; and INTAS, HCM, and TMR contributions from the European Community.

References

[1] D. De Schepper et al., submitted to Nucl. Inst. and Methods.

[2] A. Golendoukhin et al. and B. Braun et al., contributions to the 12th International Symposium on High Energy Spin Physics, Amsterdam, Sept.'96 (World Scientific, eds. C.W. de Jager et al) p.241 and p.331; and J. Stewart and B. Braun, contributions to the 7th International Workshop on Polarised Gas Targets and Polarised Beams, Aug.'97, Urbana-Champaign, to be published as AIP conference proceedings.

[3] MAFIA Userguide, Version 3.2, Computer Simulation Technology, Lauteschlogerst. 38, 64289 Darmstadt, Germany; tel. +49 6151 717057, and
M. Bartsch et al., Computer Physics Communications 72 (1992) 22.

[4] TOSCA computer program. Vector Fields Inc., 24 Bankside, Kidlington, Oxford OX5 1JE, England; tel.: (0865) 370151.

[5] M. Geijsberts et al., Nucl. Instr. and Meth. A313 (1992) 377.

[6] J. van der Marel, PhD thesis, Delft University (1997).

[7] D-263 glass is produced by Desag, Germany.

[8] J.M. Butler et al., Nucl. Instr. and Meth. A290 (1990) 122.

[9] A. Trudel, private communication; U. Becker et al., private communication.

[10] S.F. Biagi, Nucl. Instr. and Meth. A310 (1991) 133.

[11] R. Openshaw, R. Henderson, W. Faszer, and M. Salomon, Nucl. Instr. and Meth. A307 (1991) 298.

[12] F. Schmidt, Diploma thesis, Friedrich Alexander Universität Erlangen-Nürnberg, May 1996. HERMES internal note 96-043*.

[13] S. Bernreuther et al., DESY 98-011, hep-ex/9803005, submitted to Nucl. Inst. and Meth.

[14] S. Bernreuther, Diploma thesis, Friedrich Alexander Universität Erlangen-Nürnberg, 1995; HERMES internal note 95-068*.

[15] F. Neunreither, PhD thesis, Friedrich Alexander Universität Erlangen-Nürnberg, 1997.

[16] R. Veenhof et al., program GARFIELD, a drift chamber simulation program; CERN Program Library, Long Writeup, W5050, 1991.

[17] S. Bernreuther et al., Nucl. Instr. and Meth. A367 (1995) 96.

[18] D. Hasch, Diploma thesis, Humboldt Universität zu Berlin, 1995; HERMES internal note 95-028*.

[19] J.C. Armitage et al., Nucl. Instr. and Meth. A271 (1988) 588.

[20] LeCroy Research Instrumentation Catalog - 1996.

[21] E. Gärber, Diploma thesis, Humboldt Universität zu Berlin, November 1996. HERMES internal note 96-062*.

[22] T.-A. Shibata et al., accepted in Nucl. Instr. and Meth. A.

[23] W. Wander, PhD thesis, Friedrich Alexander Universität Erlangen–Nürnberg, April 1996. (English translation: HERMES internal note 97-031*)

[24] GEANT Detector Description and Simulation Tool, CERN Program Library, Long Writeup, W5013, 1994.

[25] Particle Data Group, Phys. Rev. D54 (1996) 1.

[26] The F101 glass blocks were provided by the Lytcarino factory, 140061 Lytcarino, Russia.

[27] M. Kobayashi et al., KEK Internal Report 93-178 (1993).

[28] H. Avakian et al., Nucl. Instr. and Meth. A378 (1996) 13;
A. Fantoni, PhD thesis, Universitá della Calabria, February 1996, HERMES internal note 96-015*.

[29] H. Avakian et al., accepted in Nucl. Inst. and Methods.

[30] P. Baillon et al., Nucl. Instr. and Meth. 126 (1975) 13.

[31] J.V. Emerson, MSc thesis, Simon Fraser University; July 1995. HERMES internal note 96-038*.

[32] The fibers were provided by: Carl Freudenberg Faservliesstoffe, P.O. Box 100363 Weinheim 69465. The commercial designation of the material is VILEDON C 1900/034.

[33] D.M. Thiessen, MSc thesis, Simon Fraser University; March 1996. HERMES internal note 96-028*.

[34] R.B. Kaiser, PhD thesis, Simon Fraser University; April 1997. HERMES internal note 97-017*; and
R.B. Kaiser (for the HERMES PID Group), HERMES internal note 97-025*.

[35] K. Ackerstaff, Contribution to DIS96, Rome, Apr.'96; eds. G. D'Agostini and A. Nigro, World Scientific, p.526; and "Cross-Sections for Vector Meson Production at HERMES", paper in preparation.

[36] F.A. Berends and A. Böhm, in High Energy Electron–Positron Physics, eds. A. Ali and P. Söding, World Scientific Publishing, Singapore, 1988, p. 27.

[37] Th. Benisch, Diploma thesis, Friedrich Alexander Universität Erlangen-Nürnberg, March 1994; HERMES internal note 94-030*; and PhD thesis, Friedrich Alexander Universität Erlangen-Nürnberg, March 1998.

[38] G.I. Britvich et al., Nucl. Instr. Meth. A321 (1992) 64.

[39] A.V. Antipov et al., Nucl. Instr. Meth. A327 (1993) 346.

[40] V. Samsonov, Proc. of the 'Crystal 2000' International Workshop, Chamonix, France, 1992, eds. P. Lecoq et al. (Ed. Frontières, 1993) p. 383.

* The theses mentioned in these references are available as HERMES internal notes, and can be accessed on the HERMES web pages:
http://www-hermes.desy.de/notes/

†Deceased.